Growth modes of Fe(110) revisited: a contribution of self-assembly to magnetic materials

Olivier Fruchart, Pierre-Olivier Jubert, Mustafa Eleoui, Fabien Cheynis, Bogdana Borca, Philippe David, Valérie Santonacci, Annick Liénard, Manabu Hasegawa, Claire Meyer

TOPICAL REVIEW

Growth modes of Fe(110) revisited: a contribution of self-assembly to magnetic materials

O Fruchart, P O Jubert‡, M Eleoui, F Cheynis, B Borca, P David, V Santonacci, A Liénard, M Hasegawa and C Meyer

Laboratoire Louis Néel, CNRS, BP166, F-38042 Grenoble Cedex 9, France

E-mail: Olivier.Fruchart@grenoble.cnrs.fr

Abstract. We have revisited the epitaxial growth modes of Fe on W(110) and Mo(110), and propose an overview or our contribution to the field. We show that the Stranski-Krastanov growth mode, recognized for a long time in these systems, is in fact characterized by a bimodal distribution of islands for growth temperature in the range $\sim 250 - 700\,^{\circ}\mathrm{C}$. We observe firstly compact islands whose shape is determined by Wulff-Kaischev's theorem, secondly thin and flat islands that display a preferred height, *i.e.* independant from nominal thickness and deposition procedure (1.4 nm for Mo, and 5.5 nm for W on the average). We used this effect to fabricate self-organized arrays of nanometers-thick stripes by step decoration. Self-assembled nano-ties are also obtained for nucleation of the flat islands on Mo at fairly high temperature, *i.e.* $\sim 800\,^{\circ}\mathrm{C}$. Finally, using interfacial layers and solid solutions we separate two effects on the preferred height, first that of the interfacial energy, second that of the continuously-varying lattice parameter of the growth surface.

PACS numbers: 68.55.-a, 81.16.Dn, 81.15.Fg, 75.75.+a

Submitted to: *J. Phys.: Condens. Matter*

‡ Present address: IBM Almaden Research Center, 650 Harry Road, San Jose, CA-95120, USA

Introduction

The first report of the epitaxial growth of the centered cubic element Fe along the (110) orientation was published more than twenty years ago[1]. Since that time a great number of publications have followed on the subject, with so far no sign of vanishing interest or slowing down of the discovery of new phenomena. The epitaxial growth under ultra-high vacuum (UHV) has mainly been performed on W and Mo, the two refractory metals than were shown to give rise to no or marginal interface reactivity at any temperature up that of thermal desorption[2], thus enabling one to fully explore the growth behavior. In this article we will restrict ourselves to these two metals as a growth surface.

At first the interest arose for Fe(110)/W(110) because it appeared as a favorable system for an experimental realization of a model 2D magnetic system. The reasons were that 1. Fe and W are immiscible in the bulk 2. (110) is the most dense plane of centered cubic materials, thus of *a priori* lowest surface energy and unfavorable against facet formation 3. W(110) surface energy ($\gamma_{\mathrm{W}} \sim 4.0\,\mathrm{J.m^{-2}}$) is significantly larger than that of Fe ($\gamma_{\mathrm{Fe}} \sim 2.4\,\mathrm{J.m^{-2}}$), favoring wetting[3]. The immiscibility at the (110) interface was confirmed for Fe/W at all temperatures[2]. The single atomic layer (AL) was found to be pseudomorphic, and was thus a model system for calculations and analysis. The conditions are slightly less favorable for Mo, of surface energy $\gamma_{\mathrm{Mo}} \sim 3.4\,\mathrm{J.m^{-2}}$, and with alloys like Fe_2Mo and Fe_3Mo_2 reported in the bulk and for which indeed marginal reactivity was reported at the Fe/Mo(110) interface above 525 °C[2]. This explains why the thorough investigation of epitaxial growth of Fe/Mo(110) started much later[4], finally revealing a behavior very similar to the case of Fe/W(110).

In short, Fe has a misfit close to 10 % with both Mo and W. For both Fe/Mo(110) and Fe/W(110) it was reported that at any temperature the growth begins by a pseudomorphic first AL, which above room temperature completes perfectly before the next layers start to grow. Then at elevated temperature further growth proceeds in the Stranski-Krastanov mode, whereas continuous although rough films are obtained at room temperature. More in detail, the following aspects have been reported: essential interfacial inertness[2, 5], atomic diffusion (W[6, 7] and Mo[8]), the growth and structure of the first AL [1, 9, 10, 11, 12, 13], the onset of dislocation formation and the structure of the interfacial dislocation network as a function of thickness (W[1, 11, 14, 15] and Mo[4, 16, 17]), the growth of continuous films (including characterization of stress and strain relaxation (W[12, 13, 15] and Mo[18, 19]), the kinetic roughness and a procedure for its smoothening[20, 21, 22], the formation of 1 AL and 2 AL stripes by step-decoration of vicinal surfaces and as a function of miscut azimuth (W[10, 23, 24, 25]), the onset of SK growth and nanostructures obtained by annealing or directly by high temperature growth (W[26, 27, 28, 29, 30, 31, 32] and Mo[4, 16]).

Some years ago we have considered Fe(110) magnetic systems in the context of the rising interest in self-assembly, *i.e.* the process by which nanostructures (wires, dots etc) can be spontaneously fabricated by deposition on surfaces. In the following we will use the term *self-assembly* (SA) when the nanostructures display no order or only

short-range order, and *self-organization* (SO) when the nanostructures display at least a medium range order[33]. In search of optimized growth procedures for the fabrication of SA or SO Fe(110) nanostructures we have undertaken a systematic investigation of growth processes in terms of substrate material, amount of Fe deposited, growth temperature and possible annealing. In this course we have gathered significant new data about the system, and uncovered new growth phenomena. Notice that our evaporation technique is pulsed laser deposition performed under strict UHV conditions. This technique yields results very similar to those obtained by molecular beam epitaxy[34, 8]. We indeed found no *quantitative* discrepancy with previously published data.

It is the purpose of this article to summarize our contribution to growth processes of Fe on W(110) and Mo(110) surfaces. We have already published several articles fully or partly related to the epitaxial growth of Fe(110). These concerned the principle of growth of high-quality buffer layers on Sapphire[21], the sub-monolayer range for Fe/Mo(110)[8], the occurrence of self-assembled Fe/Mo(110) compact islands and the deduction of the effective interfacial energy for this system[35, 36], the fabrication of nanometers-thick stripes by step decoration for both Mo(110) and W(110) surfaces[37, 38, 39]. The present article aims at giving an overview of our results, therefore some overlap with the above-cited articles is inevitable. Nevertheless we report here more details and new results. Besides, we report preliminary results using a more systematic approach. The first improvement consists in tuning continuously the in-plane lattice parameter from that of W to that of Mo, using solid solutions. The second improvement consists in controling independently from the previous point the chemical nature of the interface, either W or Mo, making use of ultrathin pseudomorphic interfacial layers. Applied to the subsequent fabrication of both islands or wires, this approach should in the future cast light on the relevant parameters involved in the process of self-assembly of Fe(110). Incidentally, this latest investigation has allowed us to further increase the versatility of Fe(110) nanostructures that can be grown.

1. Experimental procedures

The experimental growth setup has been significantly modified since its lastest description[35, 8] so that we describe it here in detail. It consists of three interconnected UHV chambers, each equipped with an ion pump with a Ti sublimator. The first chamber is used for samples and targets storage, and samples preparation and analysis. It is equipped with a scanning Auger electron spectroscopy with MACII analyzer, scanning Argon ion etching (Thermo VG EX05), substrates outgassing (base pressure $2-3\times10^{-10}$ Torr). A turbo pump is directly fitted to this chamber for use during ion etching. The second chamber is equipped with a room-temperature Omicron STM-1 Scanning Tunneling Microscope with a maximum field of view of 800 nm (base pressure 5×10^{-11} Torr). The growth proceeds in the third chamber (base pressure 5×10^{-11} Torr). The evaporation method is pulsed-laser deposition (PLD) using a Quantel Nd-YAG frequency-doubled ($\lambda=532$ nm) laser with pulse width around 10 ns,

a shooting frequency of 10 Hz and a maximum energy per shot of 150 mJ. The energy is adjusted by tuning the delay between the oscillator and the amplification stage of the laser while the pumping stays constant. The growth chamber is equipped with a 10 kV RHEED setup with a 10-bit CCD camera synchronized with laser shots, so that RHEED patterns and oscillations can be monitored during deposition. The laser beam enters the chamber through a window and impinges on the target at an angle 27 ° away from the normal to the surface. The main parameter for evaporation is the fluence F, *i.e.* the energy per shot and per unit area of the target[40, 41, 34]. F can be adjusted with both the laser power and a focusing lens located outside the chamber on the beam path. The focal length of the lens is 500 mm. The focus is located *ahead* of the target, at a distance $120 - 180$ mm depending on the element to evaporate. The resulting working value lies in the range $0.1 - 1\,\mathrm{J/cm^2}$, yielding a typical deposition rate of 0.5 Å/mn. The laser is rastered on the target with the help of an *ex situ* mirror mounted on an electro-acoustic device. The substrate-to-target distance is 140 mm. A Cu foil placed before the sample can be moved continuously during deposition to mask part of the sample and thus fabricate wedge-shaped films, *i.e.* films whose thickness is varied from one place to another on a sample. In the case of simple wedges the direction of the movement of the mask is always progressively masking the sample. By rotating the sample around its axis by 180 ° a wedge with an opposite slope can be fabricated. To switch over to another target the beam can be stopped with an *ex situ* mechanical shutter, another target is moved in front of the beam, and the focusing of the beam on the target is adjusted to a value suitable for each material. All these movements are motorized and controlled through a computer that allows one to launch macros, like the numerous opposite wedges necessary for the fabrication of solid solution buffer layers with continuously varying in-plane lattice parameter, as reported in the next section. The location on the wedge of the focused electron beam used for AES can be precisely and reproducibly controlled owing to a translation stage. The convolution of the translation uncertainty and the size of the spot on the sample is estimated to yield an uncertainty of 100 μm. For quantitative AES the measurements are normalized to the beam intensity, which is measured regularly during each series of measurements on a reference part of the sample consisting of either a thick deposit or a bare buffer layer of a pure element.

All our film are deposited on commercial Sapphire Al_20_3 wafers. Wafers from several suppliers have been used (Union Carbide, Bicron, Crystal GmbH), without noticing significant differences on the crystal quality of the films grown on top. The miscut was found to vary from wafer to wafer, however is unchanged over the two-inch area. Typical values lie below 0.1 °. The sample holder consists of a modified one inch Riber *Molybloc* with a slot to insert an Omicron STM holder. One of the clamps holding the substrate is rotated *in situ* with the Omicron wobblestick to scratch the surface of the sample and set an electrical contact for STM measurements. Openings have been made in both the molybloc and the STM sample holder, so that the rear of the substrate is in direct view of a Joule-heating filament. With this setup the sample size is 6.5×8.5 mm, sitting on a

500 μm-wide ledge. To sit on this thin ledge the two-inch Sapphire wafers are precisely laser-cut in a dedicated *ex situ* chamber. To this purpose the Nd-YAG laser is focused on the backside of the wafer, with a spherical lens $f = 200$ mm. A set of two cylindrical lenses with identical flat axes, one convergent and one divergent however with shifted focal planes, is inserted before the focussing spherical lens. This provides us with a beam with a very elongated elliptical shape, in turned transformed with a diaphragm into a very narrow and nearly rectangular shape on the wafer, whose feature is a nearly constant energy per unit *length*. With this design the wafer is cut much more efficiently than with a simple spherical focusing, because laser ablation suffers from a saturating effect above the evaporation threshold[40]. The linear cutting speed is then of the order of one millimeter per second. The wafers are then cleaned in an ultrasonic bath in 10-20 % diluted RBS25 (Chemical Products, Belgium), then rinsed with deionized water, to remove the Al deposited at the back during the laser cutting. The rear of the wafer is sputter-coated by sputtering prior to deposition with a 100 nm-thick layer of a refractory metal, usually W. The purpose of this layer is to absorb most of the heating radiation emitted by the filament on the deposition stage. Without this layer a significant amount of radiation is absorbed directly by the epitaxial film, resulting in higher and uncontrollable temperatures. Substrate temperatures up to 950 °C can be achieved with this setup, calibrated by an optical pyrometer and controlled routinely by a thermocouple in direct contact with the rear of the molybloc. Owing to this indirect measurement of temperature, error bars on temperature reading might be significant, especially in the range $25 - 250$ °C because of thermal inertia. The sample can also be substituted with a quartz microbalance. Finally all deposits are capped before taking them back to air. The capping, deposited at room temperature (RT), may consist of 5 nm of Mo or W, or of a few atomic layers of either covered by a 2 nm of Al, Mg or Au. The latter two are slightly annealed above room temperature to smoothen the surface. All these capping procedures have been checked to result in a smooth layer displaying single atomic steps, and are an efficient barrier against oxidation of Fe.

Atomic force microscope images were performed on a Park Scientific Instrument Autoprobe CP in contact or non-contact mode. The Si tips are pyramidal (Mikromasch CSC21B, force constant 2 N/m). X-ray diffraction (XRD) was performed using several setups equipped with a monochromator. We worked essentially in a $\theta - 2\theta$ geometry, probing either diffusion vectors out of the plane, or in-plane with a grazing incidence. In the following misfits are expressed with respect to the growing film, *e.g.* $\epsilon = (a_{\mathrm{Mo}} - a_{\mathrm{Fe}})/a_{\mathrm{Fe}}$. Finally, for element A grown on B we use the notation A/B.

2. Growth of buffer and interface layers

We do not use metal single-crystals as a substrate, but instead we grow bcc(110) buffer layers on Sapphire $Al_20_3(11\overline{2}0)$. On the one hand this is more time-demanding than using metal single crystals as a new buffer layer has to be prepared for each new sample. On the other hand it allows one to keep all samples and take them *ex situ* for further

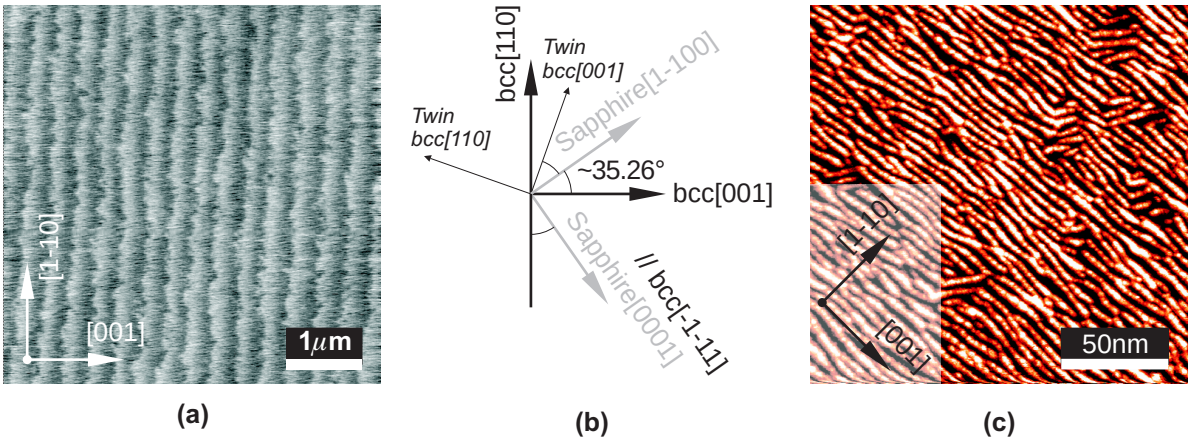

Figure 1. (a) $5 \times 5\,\mu$m AFM image of a typical $Al_20_3(11\bar{2}0)$ surface displaying an array of monoatomic steps after annealing at 800 °C for one hour under UHV. The vertical scale is 4 Å (b) epitaxial relationships between Sapphire and body centered cubic elements (bcc), revealed by XRD and RHEED. The majority relationship[43] is marked with dark lines and upright letters, while the minority twin is marked with thin lines and italicized letters (c) The size of the crystallites of the minority twin are revealed in real space by STM by the areas with a 70°-rotated grooved pattern formed upon deposition at moderate temperature, see text.

characterization after growth. Most importantly, this allowed us to vary the composition and thus tune the in-plane lattice parameter, as will be shown in the following. We reported in the past the growth of high-quality single-crystalline Mo(110)[21] and Nb(110) buffer layers[42]. After recalling the growth procedure of such layers and give further characterization with respect to Ref.[21], we present three improvements that have been of use for the growth studies of Fe(110) reported here, namely the successful suppression of twinning for W(110), the fabrication of solid solutions with tunable in-plane lattice parameter, and the deposition of atomically-flat pseudomorphic ultrathin layers over these buffer layers.

2.1. Recall of the general procedure

The Sapphire wafers, prepared as reported above, are mounted on sample holders and outgassed under UHV at 800 °C for one hour and let cool down for one hour. At this stage the crystal surface consists of atomically-flat terraces separated by single atomic steps, whose separation and orientation are related to the residual miscut (Figure 1a). The miscut was found to vary from wafer to wafer, however is unchanged over the two-inch area. A typical value for the terrace width is 200 nm (see FIG.1a,2f).

Buffer layers consist of bcc materials deposited on Sapphire. The growth process described in the following applies equally well for Mo, Nb and W, at least. The epitaxial relationship with Sapphire agrees with that reported already long ago[43] (Figure 1b). These bcc materials are first deposited at moderate temperature. In the past we were starting the growth at room temperature (RT) and the heater was switched on around

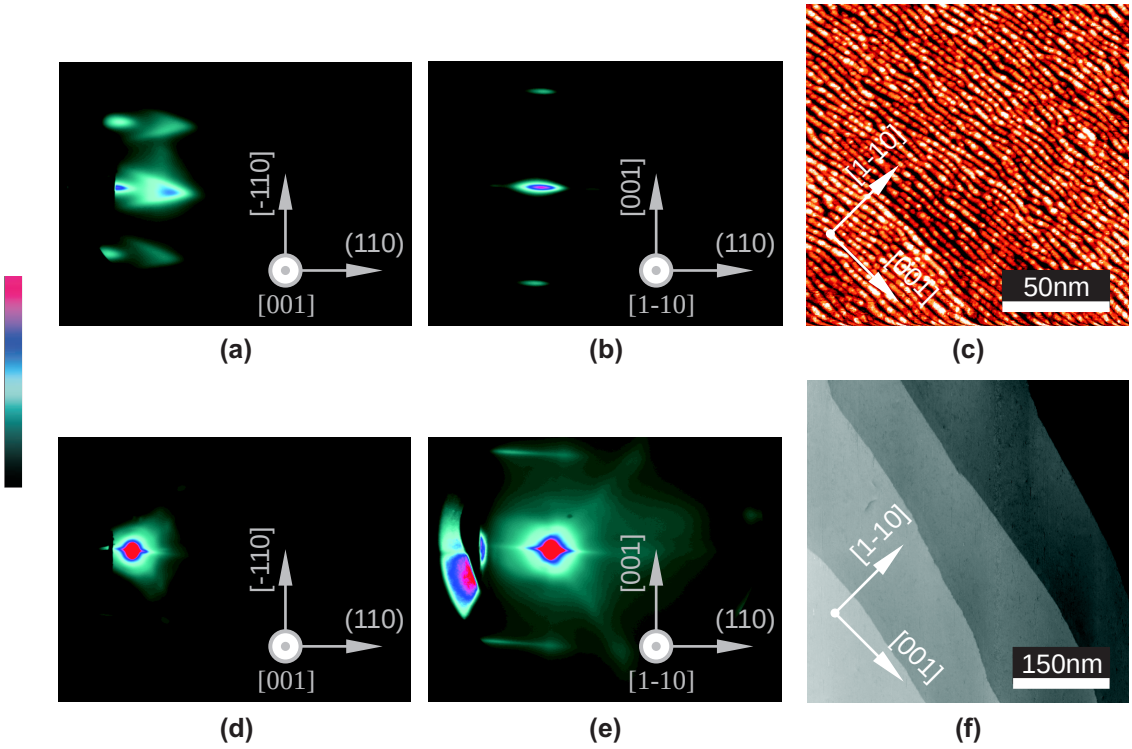

Figure 2. Characterization of Mo(110)/$Al_20_3(11\bar{2}0)$ films (a-c) after deposition at room temperature and (d-f) after deposition at room temperature followed by annealing at 800 °C. (a-b;d-e) RHEED patterns along two azimuths (color scale on the left). The sample lies vertical at the left of the screen. (c,f) STM images.

$0.5 - 1$ nm to reach $150 - 200$ °C by 1.5 nm. We nowadays perform the entire growth at RT, with no detectable difference in the quality of the final annealed films, see next paragraph. Concerning the films before annealing, RHEED and STM show that after growth at moderate temperature their surface is rough (Figure 2a-c), displaying grooves oriented along [001], a common feature for bcc(110) epitaxy[20, 21, 22]. The microscopic origin of this anisotropy of roughness has been discussed in Ref.[20] and simulated in [22], on the basis of anisotropic diffusion at the nucleation stage, followed by a kinetic effect related to the Schwoebel barrier. In the former article the angle of the facets was investigated for Fe(110) for a few thicknesses up to $\Theta = 9$ AL, at 200 K. It was found that this angle increases during deposition to reach a value close to 18 °. The authors could nicely reproduce their data with a model of layer-restricted-diffusion (LRD) growth. Our data partly confirm these conclusions. The arrow-like pattern of Figure 2a is blurred at the beginning of growth and sharpens upon deposition. However, whereas a LRD model predicts a steady increase of the mean angle upon growth, we evidence that the angle of the facets becomes stationary after some nanometers are deposited. RHEED and STM show in quantitative agreement that the stationary angle is close to ± 19 °, coherent with facets of type {210} (see Appendix II). These values are consistent with the thickest deposits of Albrecht *et al.* dealing with Fe[20], although these authors did

not realize that a stationary value had been reached. The breakdown of the continuous LRD model may be due to a modification of the Schwoebel barrier, and/or to the modification of diffusion rates on the micro-terraces of the facets of type {210}, due to finite size and/or the discreteness of the terrace. Indeed the width of such a terrace is $\frac{7}{2}a_{\rm bcc}\sqrt{2}/2 \simeq 7-8\,$Å, and only three atomic rows sit on each terrace. In fact in Ref.[22] it was already suggested that some type of facet should be stabilized, using geometrical arguments for impinging and diffusing atoms. However it was claimed that the {310} facets should be stabilized, contrary to our findings. The stability of the {210} facets has a positive effect on the array of grooves, whose distribution of local orientation and period decrease upon further deposition after the nominal facet angle has been reached on the average, *i.e.* after $1-2\,$nm. The array progressively thus becomes self-organized, see Figure 3.

The facetted grooves form upon deposition at temperatures below 225 °C[21] for Mo and 325 °C for W. We have recently evidenced with RHEED that the roughness becomes isotropic below approx. 100 °C for W. A similar lower bound is likely to exist for Mo and Fe, however shifted below RT in relation with the hierarchy of bonding strengths. In Ref.[20] facets were still observed for Fe at 150 K. As our setup cannot operate below RT we could not confirm this hypothesis. Nevertheless, the existence of a range of temperatures for the kinetic formation of grooves, and its quantitative determination for W, should be a valuable input for simulations, to determine the microscopic mechanism responsible for this growth phenomenon. These grooves may for instance be a valuable template for the self-organization of wires, like those obtained upon grazing-incidence ion etching[44, 45, 46]. With this in mind, let us add that STM investigations revealed that the order seems to be at its best somewhere in the intermediate range of temperatures, in terms both of alignement of the wires along [001], and of regular period along $[1-10]$. The quality of the order is then reflected by the occurrence of a superstructure on the RHEED patterns (Figure 3). The period deduced from RHEED is in accordance with the period observed by STM, *i.e.* around 5 nm for Mo or W deposited at 100 °C (Figure 3). The average depth of the grooves is 1 nm in this case. In Ref.[20] it was postulated that the period is selected during the nucleation stage in the sub-atomic layer range of deposition, and accordingly was found to increase when the temperature of deposition was increased. Although we have not investigated this feature extensively, we have noticed that both nucleation and growth temperatures play a role. Notice finally that all crossover temperatures between different growth modes may depend on the deposition temperature, and concerning PLD depend also on the laser ablation parameters. For instance, rather smooth films can be achieved at a temperature lower than the cross-over one for a higher laser fluence, which is explained by the higher mobility of adspecies when they impinge on the surface[8]. For an overview of differences between Molecular Beam Epitaxy (MBE) and PLD see Ref.[34].

As already reported[21], there exists a dual epitaxial relationship of refractory metals with $Al_20_3(11\overline{2}0)$, both sharing bcc[111] $\parallel$ Al_20_3[0001]. The dominant relationship is bcc[001] $\sim\parallel$ $Al_20_3[1\overline{1}02]$[43], associated with intense streaks on RHEED,

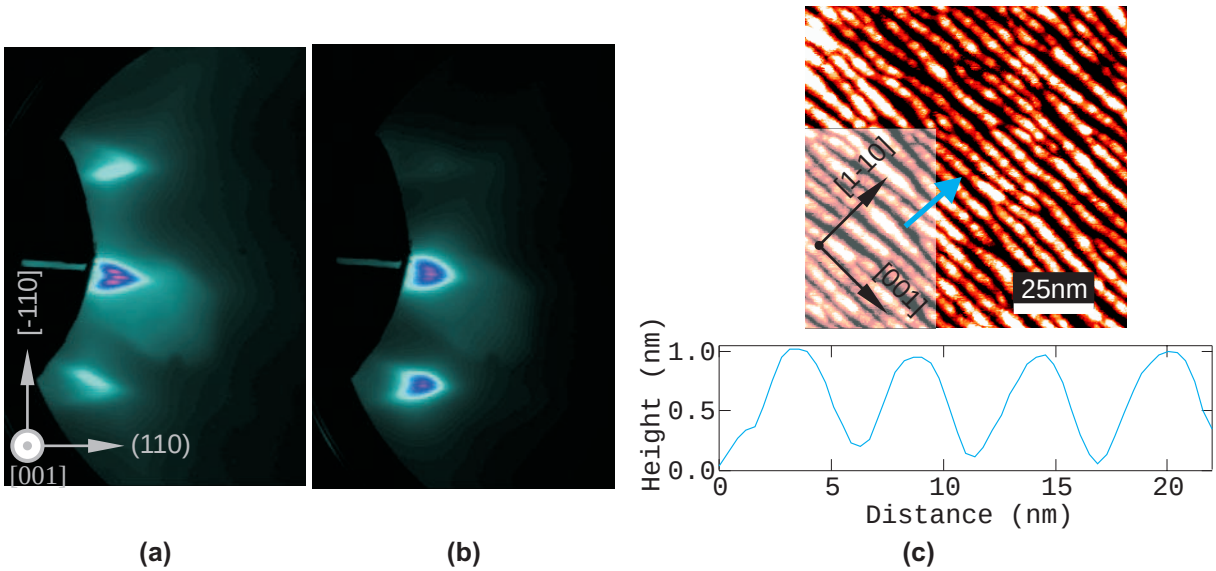

Figure 3. RHEED patterns on a grooved surface arising upon deposition of W(110) at 100 °C, along the (a) [001] azimuth (b) same as a, misoriented by °1 away from [001] so as to enhance the satellite structure of the $[1-10]$ arrow-like streak (bottom). (c) STM image of the W(110) surface with a cross-section (arrow on the image).

whereas weaker streaks on the RHEED pattern can be attributed to a 70 ° in-plane rotated relationship, in other words mirrored with Sapphire $(1\bar{1}00)$ plane. This was confirmed by grazing incidence XRD. The dual relationship is explained by the initial completion of the dense atomic rows along bcc $< 111 >$ directions in the nucleation stage, followed by the completion of $< 100 >$ directions of atoms at $\approx \pm 35.26$ ° on either side. The crystallites of the minority twin crystallites are easily revealed upon growth at moderate temperature from the local direction of the grooved pattern (Figure 1c). For Mo the minority crystallites cover an area not exceeding 10 % of the surface, with a typical lateral size of 15 nm.

These layers are then annealed at 800 °C for 30 min to flatten the surface and improve the crystalline quality. RHEED patterns then display a sharp 1×1 pattern, and reveal that the minority twin has vanished in the case of Mo, however not in the case of W (upon a similar annealing the minority twin vanishes in the case of Nb and V layers, however not in the case of Ta. These three buffer layers have not be used for the overgrowth of Fe reported here). In the case of Mo the disappearance of twins can also be checked by redeposition of a bcc material at moderate temperature, in which case the array of grooves, locally aligned along [001], consists of one single domain. It is this procedure that has been used for Figure 2a-c. In Ref.[47] it was reported that Mo films deposited at 800 °C do not show this problem of twinning, however displayed a weak misorientation of crystallites in the as-deposited state, resulting in micro grain boundaries. It was shown using Low-Energy Electron Microscopy that these grain boundaries could be largely eliminated by annealing at 1425 °C as they then become

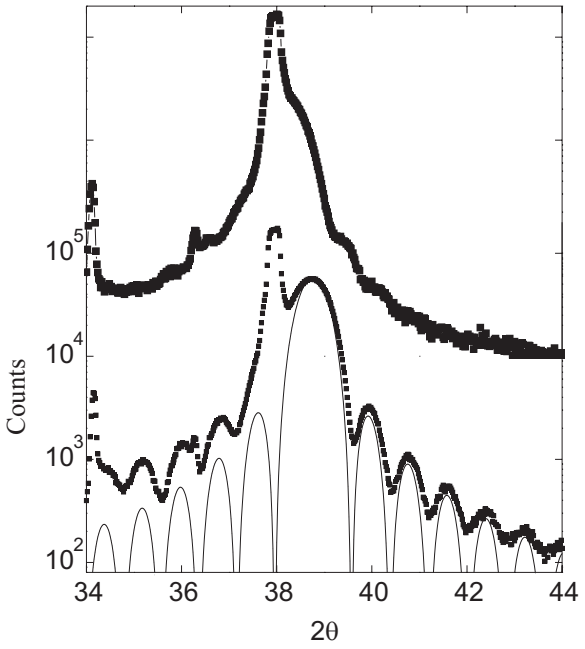

Figure 4. XRD in the $\theta-2\theta$ geometry of a Nb film grown at 200 °C (top) and annealed at 800 °C (down). The dots stand for experimental points, while a qualitative fit of the Kissing fringes a shown in continuous line for the latter.

very mobile. In our case we never came upon any evidence of the existence of such micro-grain boundaries, in particular with STM. These annealed buffer layers consist of atomically-flat terraces separated by mono-atomic surface steps (Figure 2f). Large scale *ex situ* AFM images show that these steps form a long-range ordered array on the sample, whose orientation and period are linked with the residual miscut of the wafer after polishing. Over a large number of wafers from various manufacturers the terrace size was found to vary from 100 nm to 400 nm, thus implying an average miscut angle around 0.05 °. Notice that the miscut was always found to be uniform over the entire two-inch wafer. Thus, as this wafer is cut into tens of sub-centimeter-size sub-wafers, once the miscut angle and azimuth are known from microscopy, spare sub-wafers are stored that can be used whenever a desired miscut is required.

The annealed buffer layers were characterized *ex situ* with X-rays. The measurements with the highest resolution were performed in the $\theta - 2\theta$ geometry to measure the out-of-the-plane q vector. No detectable deviation from the bulk lattice parameter was evidenced, within the accuracy of better than 0.1%. Kissing fringes with many orders are observed only after annealing, resulting from the finite thickness of the layer, confirming the flatness of both interfaces (Figure 4). For all films the crystalline coherence length equals the film thickness minus a few atomic planes that contribute to an amorphous oxyde layer at the free surface. In grazing incidence the epitaxial relationship was confirmed and the bulk lattice parameter was retrieved, within the experimental accuracy of 0.5%.

The deposition and annealing parameters are not critical to get these buffer layers

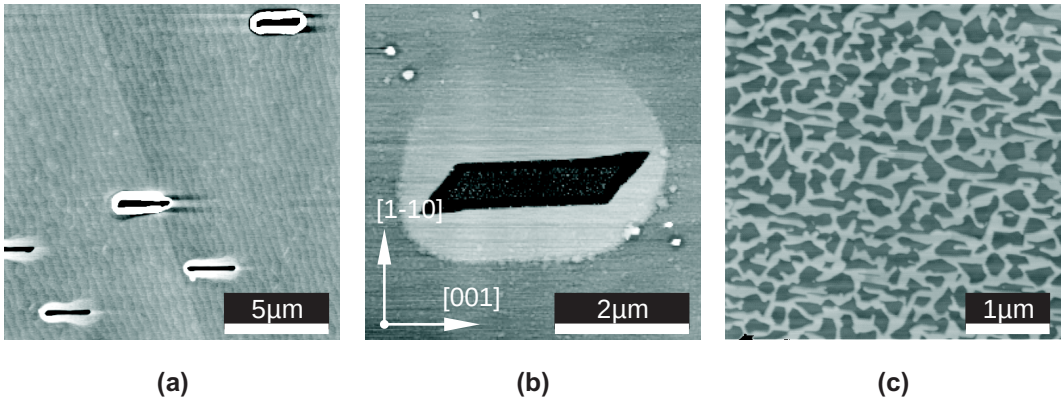

Figure 5. Unwetting of Mo(8 nm)/$Al_20_3(11\bar{2}0)$. (a) After annealing at $900 \pm 50\,^{\circ}$C. The array of monoatomic steps of Mo can be seen at the background. (b) same conditions, with now the atomic steps running along [001]. The steps are not clearly seen because the scan was performed along the same direction. On both pictures the hole created by unwetting is decorated by a brim of Mo, with a flat surface, such that it appears as wedged over the slightly vicinal continuous Mo buffer layer. The small irregular patterns, looking like islands, are Al islands arising from a protective layer deposited under non-optimized conditions. (c) A Mo film of nominal thickness $\Theta = 2.2$ nm, which upon annealing at $900 \pm 50\,^{\circ}$C unwets Saphir while forming nanostructures of height ~ 5.5 nm.

of high cristalline and topographic quality. However a minimum nominal thickness $\Theta = 8$ nm is required to avoid the unwetting of the substrate during annealing at $800 \pm 50\,^{\circ}$C. The Mo layers start to unwet sapphire for annealing temperatures above $900 \pm 50\,^{\circ}$C or $\Theta < 8$ nm (Figure 5a) and complete unwetting occurs for a significant overpassing of these parameters (Figure 5). We checked that 50 nm-thick buffer layers were stable up to at least $1200\,^{\circ}$C, in agreement with similar layers fabricated with MBE[47]. Such buffer layers are now used by other groups for the deposition of magnetic materials and nanostructures based on Fe(110)[48, 49, 50, 51].

To conclude, the (110) layers deposited under the optimized procedure described above are of high crystalline and topographic quality and are nearly indistinguishable from clean surfaces of metal single crystals.

2.2. Suppression of twinning for W

It is important to eliminate the minority twins of W(110)/Al_20_3 to raise the quality of these layers to the level of those of Mo, Nb and V. We indeed observed that Fe dots grown on a twinned surface display features rotated by $70\,^{\circ}$ with respect to the expected [001] direction, as a result of nucleation on the minority twin.

We could eliminate the minority twin by a so-called *dusting* procedure: a small amount of Mo is deposited first on Sapphire at room temperature, then W is deposited following the procedure described above. RHEED reveals that after the growth of the dusting Mo plus W twins are present, like in the case of pure elements deposited under

identical conditions. However this time the twinning vanishes upon annealing (same procedure as above). The complete elimination of the twins was confirmed by grazing-incidence X-rays and STM images of W overlayers deposited at moderate temperature on annealed W(8 nm)/Mo/Al_20_3buffer layers, similarly to the example shown on Figure 2a-c. It was found that as little as 0.6 nm is enough to suppress the twinning. We did not attempt to determine the lowest required amount. The impact of ultrathin dusting layers on the initiation of growth had been reported previously, *e.g.* 0.6 nm of V deposited on MgO(001) are enough to change the growth of NiMnSb from polycrystalline to epitaxial[52]. In our case the role of Mo in easing the recovery of a single crystal through annealing has not been investigated. It might be to reduce the grain size of the minority twin.

2.3. Solid solutions

Lattice misfit is a key parameter in driving epitaxial growth modes. Thus it would be desirable to continuously tune the misfit, which of course cannot be realized with pure elements. The fabrication of bcc(001) buffer layers by codeposition of V and Nb was reported, which allowed the authors to tune the in-plane lattice parameter of buffer layers in the full range between that of V ($a = 3.02$ Å) and that of Nb ($a = 3.30$ Å)[53]. We have developed a process that allows us to fabricate a *chemical-gradient layer* (CGL), *i.e.* a buffer layer whose composition varies continuously from one end to the other end of the wafer. In the present paper we focus on CGL made of mixtures of Mo and W, with bulk lattice parameters 3.147 Å and 3.165 Å, respectively. The process is the following. Under the conditions detailed in section 2.1 we deposit sequentially W and Mo with the shape of opposite wedges, with an area of pure element on each side (Figure 6a). The growth temperature protocol is identical to that used for pure layers. The thickness of each bilayer is routinely 1 Å, although periods of 1 nm have been also used. The time required for the deposition of a full CGL is doubled with respect to a pure-element layer, and reaches approximately four hours. Extra time is indeed required to adjust the deposition parameters from one wedge to the next, consisting in closing the beam stop, changing of target and of laser focusing on the target, rotating the sample by 180 ° to alternate the direction of wedges, resetting the position of the mask, and opening the beam stop. This procedure is fully automated and controlled through a computer.

Upon this deposition procedure performed at moderate temperature a dual epitaxial relationship is evidence with RHEED, as with pure elements. Similarly to the case of W layers the minority twin can be completely eliminated upon annealing, provided that a dusting layer of Mo is deposited prior to the multilayer. After annealing the RHEED then displays a sharp 1×1 pattern. STM reveals a mono-atomic-stepped surface, similar to that of pure elements (Figure 2f). $\theta - 2\theta$ XRD was performed along the out-of-plane direction on several narrow slabs of these CGL. The out-of-plane lattice parameter varies indeed from that of W to that of Mo. It is expected that the in-plane lattice parameter undergoes also a linear variation.

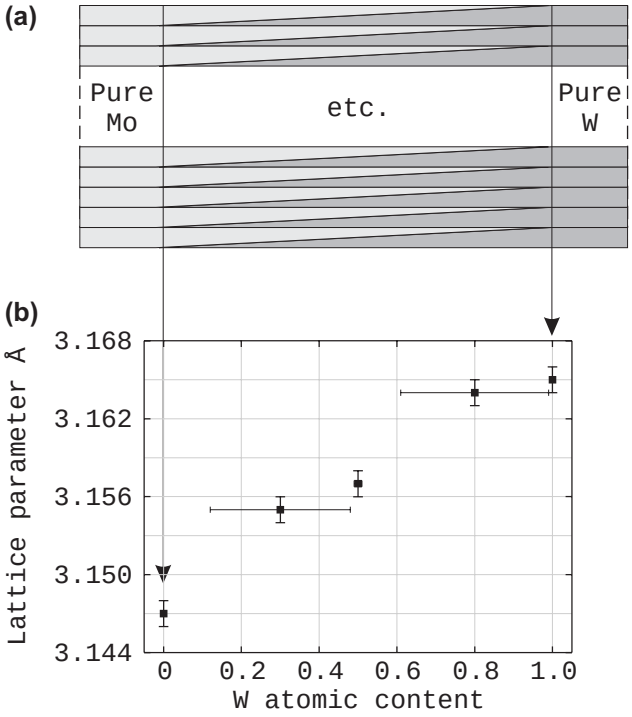

Figure 6. (a) Schematic drawing of the geometry of a Chemical-Gradient Layer (CGL) (b) Out-of-plane lattice parameter of a Mo-W CGL. The vertical bars stand for experimental uncertainties, while the horizontal bars stand for the spread of composition on the slab measured related to the finite size of the area of CGL probed.

Although these CGL are fabricated by a multilayer process, a fine intermixing is expected owing to several arguments: the sub-monolayer period, the moderate deposition temperature, the small lattice misfit and the total solubility of W-Mo. Accordingly we refer to these buffer layers as *solid solutions* throughout the manuscript. Preliminary results suggest that the process works also finely for CGL made of Nb and Mo, two elements that also mix as solutions and form no alloys with specific stoichiometry in the bulk. In this case RHEED suggests a flat surface of high quality, with an in-plane lattice parameter continuously varying across the CGL. The process should be extended in the near future to (V,Mo) CGLs, with a view to spanning the in-plane lattice parameter of buffer solutions in the entire range $[3.02 - 3.30\,\text{Å}]$.

2.4. Pseudomorphic interfacial layer

The chemical nature of the interface is another key parameter in determining growth modes in epitaxy. Ideally, it is desirable to control the chemical nature of the supporting surface independently from the in-plane lattice parameter. To achieve this we have optimized a growth process to fabricate an ultrathin pseudomorphic layer of either Mo or W on the buffer layers previously described. We illustrate this procedure in this section for W deposited on Mo(8 nm). A wedge of W is deposited at RT on a flat Mo buffer layer, followed by annealing at increasing temperatures up to 700 °C. Auger

spectra of the low energy peaks of W and Mo were taken at RT after growth and after each step of annealing (Figure 7a-d). A quantitative analysis of the spectra in the range $130-240\,\mathrm{eV}$ suggested that upon annealing no change occurs in the relative intensity of both elements upon the entire range of thickness (Figure 7e). It is reasonable to assume that no intermixing occurs upon RT deposition, first because of the high temperature of melting of both elements, second because they have a similar atomic radius making exchange processes not clearly favorable, and third because (110) is a dense plane of the centered-cubic structure. Thus we assume that the spectra after deposition are a reference for a sharp interface. This is confirmed by the nearly exponential decay of the Mo intensity as a function of W thickness. Auger spectra do not show significant changes upon annealing, which suggests that the interface with Mo remains sharp, and that no diffusion of Mo to the free surface occurs. This point is essential to control the chemical nature of the interface. Finally we checked by STM that the surface resulting from annealing was flat at the atomic scale. For subsequent growth of Fe we used layers of thickness in the range $3-5\,\mathrm{AL}$, where it is expected that the layers remain pseudomorphic thanks to the lattice misfit between Mo and W being smaller than 1%. This point could no be checked directly due to the limited resolution of RHEED.

3. Overview of growth processes of Fe/bcc(110)

As recalled in the introduction, a large number of reports have already been made concerning the UHV growth modes of epitaxial Fe(110), mainly on W and more recently on Mo. Both cases were reported to be very similar, being of Stranski-Krastanov (SK) type with one single AL of wetting. Continuous films were successfully fabricated by RT deposition followed by moderate annealing, or by rising the temperature during deposition. Nanostructures were observed to form upon annealing at higher temperature or direct deposition at high temperatures.

We have uncovered that the SK mode is in fact characterized by a bimodal distribution of islands (Figure 8). The first type consists of compact islands (*i.e.* islands with all three dimensions of the same order of magnitude) that grow nearly homothetically during deposition, and whose shape can be understood on the basis of the Wulff-Kaischev geometrical construction (see [54] and included references). The second type consists of flat and thin islands (the ratio of lateral over vertical size can exceed 100), which display a nearly mono-disperse height that depends very little on deposition conditions nor on the lateral size of the islands. We already reported this bimodal growth mode for Fe/Mo(110)[35]. In the present manuscript we report it for the case of Fe/W(110), Fe on bcc(110) solid solutions, and as a function of the independently-controlled chemical nature of the interface. We also report the dependence of the bimodal growth features upon growth conditions, island density, shape and ratio of the two types. We have also tailored the growth of the flat islands to fabricate nanometers-thick stripes that are self-organized by step-decoration at the atomic steps of the buffer-layer. This is a fundamental advancement in self-organization as, up to

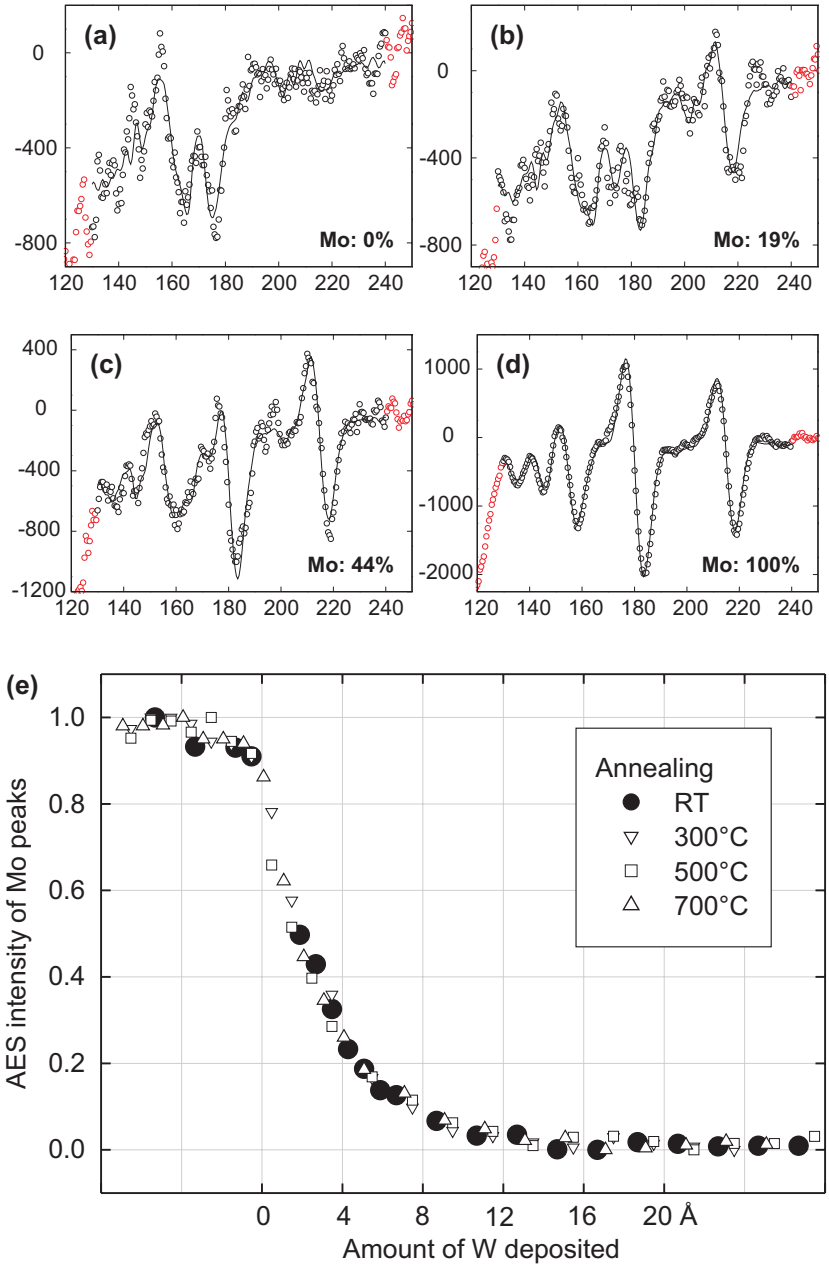

Figure 7. (a-d) Selected AES spectra performed at RT in the range [120 – 250eV], of a wedged deposit of W on a smooth Mo(110) buffer layer (normalized arbitrary units). Experimental data (dots) are fitted in the range [130 – 240eV] with a linear combination of Mo and W reference spectra (line). The fitted contribution of the Mo reference spectrum is shown in inset (e) Intensity of the Mo spectrum as a function of the coverage of W, up to above 2.5 nm, and following various annealing

now and to our knowledge, only single- or double-AL stripes could be produced by step-decoration[55, 24, 23, 56]. We already reported the growth of such stripes on pure buffer layers[37, 38] and pure buffer layers covered with ultrathin pseudomorphic interfacial layers[39]. Here we also report the growth on buffer layers of solid solution to get a better insight in the physical origin underlying the bimodal growth. All these findings allow us to draw an enlarged panorama of growth processes of Fe on cc(110) surfaces as a function of amount of material deposited, temperatures of growth and possible annealing (Figure 9). On Figure 9 areas that had not been investigated quantitatively in the literature prior to our reports are illustrated with a picture of the resulting system. The reason why these areas had been previously overlooked may come from the fact that studies on Fe(110) were already at the level of surface science when the interest in self-assembly arose. Thus studies were undertaken by STM, restricting the study to small lateral scales and amount of deposited material. Under these conditions it is not obvious to recognize the bimodal feature of growth, which on the other side is straightforward with AFM on a larger lateral scale. A discussion of the existing literature of the SK growth with respect to our data on the bimodal growth is proposed at the end of the manuscript, with a view to identifying whether the two types of islands had already been observed, however not identified as being of a different nature. Finally, although we evidenced no discrepancy between any of our data and the existing literature of Fe(110), concerning films or nanostructures, a difference of behavior between PLD (our technique) and MBE in the newly explored processes cannot be excluded.

4. Compact Fe islands

4.1. Overview

In the approximate range of temperature $325 - 575\,^{\circ}\mathrm{C}$ compact Fe islands are formed upon deposition on Mo(110) and W(110) (Figure 8). The areal density decreases with temperature, from $\approx 0.5\,\mu\mathrm{m}^{-2}$ at $325\,^{\circ}\mathrm{C}$ to $\approx 0.05\,\mu\mathrm{m}^{-2}$ at 575 K for a nominal thickness $\Theta \approx 5\,\mathrm{nm}$. This density increases very little in the range $\Theta = 1 - 10\,\mathrm{nm}$, so that the mean dimensions of the dots scale roughly with $\sqrt[3]{\Theta}$, ending up in a range of length $100\,\mathrm{nm} - 1\,\mu\mathrm{m}$ (Figure 10). On this figure it can be seen that the distribution of mean size is significant from one sample to another. This suggests that the nucleation of dots does not depend solely on growth temperature but may also depend on extrinsic parameters such as step density and orientation[57] or residual contaminants at the surface.

A closeup view of the dots reveals that they are facetted, and elongated along [001] (Figure 8b,d). The smoothness at the atomic scale of the top facet can be checked directly with AFM, with often no or only very few single atomic steps. No emerging screw dislocation has ever been observed either by this mean. The tilted facets are probed by RHEED in the form of tilted diffraction streaks, each perpendicular to one set of facets (Figure 11). The tilt angle of the facets is inferred directly from these

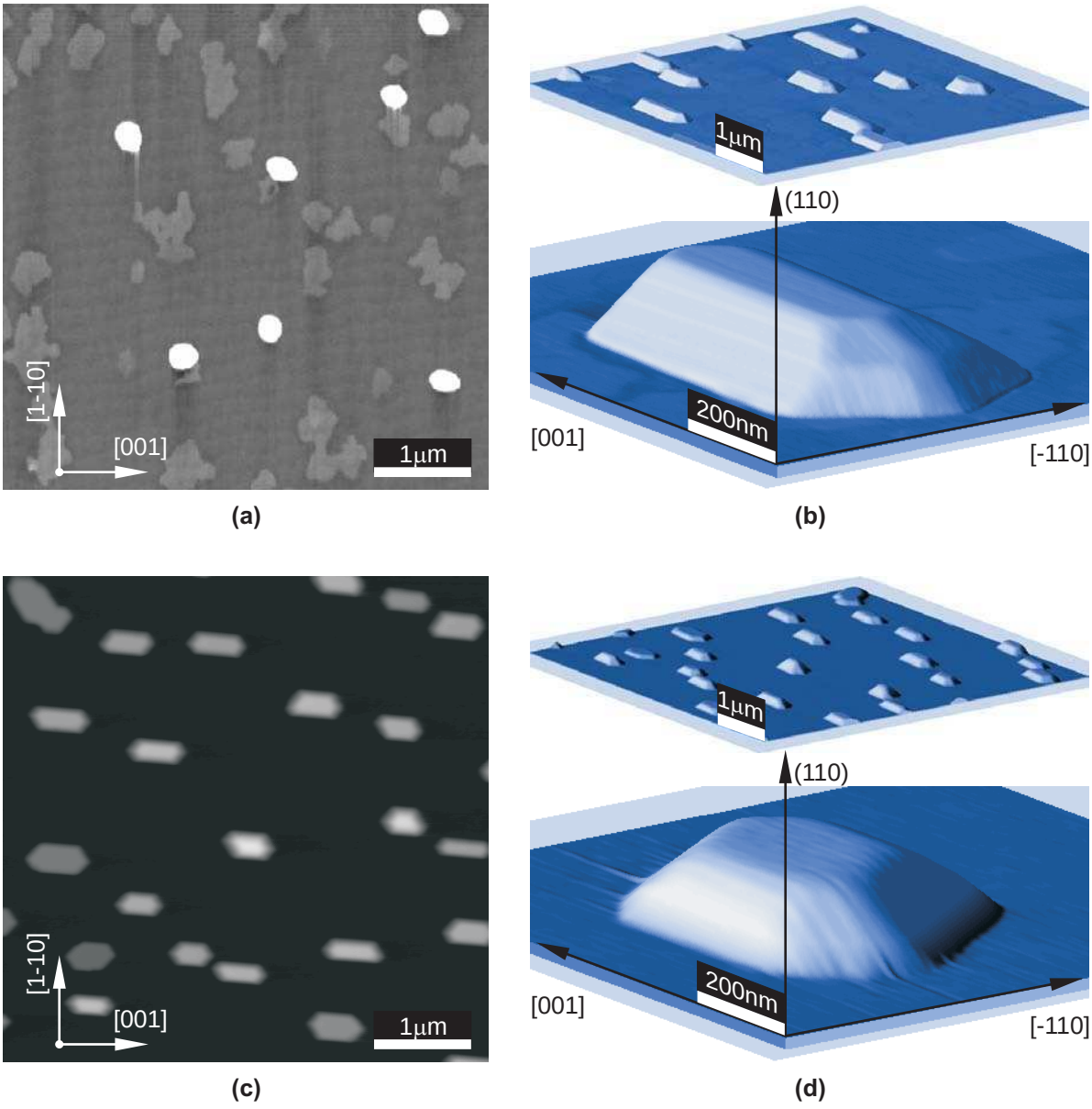

Figure 8. Illustration of the growth of Fe on (a-b) Mo(110) and (c-d) W(110). (a) Deposition of $\Theta = 0.4\,\text{nm}$ (early stages of growth) on Mo(110) at 450 °C The grey scale is chosen so as to highlight the bimodal growth mode (b) 3D view and closeup view of Fe/Mo(110) compact dots, deposited on Mo(110) at 500 °C, nominal thickness 2.5 nm (1:1 vertical scale) (c) Deposition of $\Theta = 2.5\,\text{nm}$ on W(110) at 450 °C (d) 3D view and closeup view of Fe/W(110) compact dots as in (c).

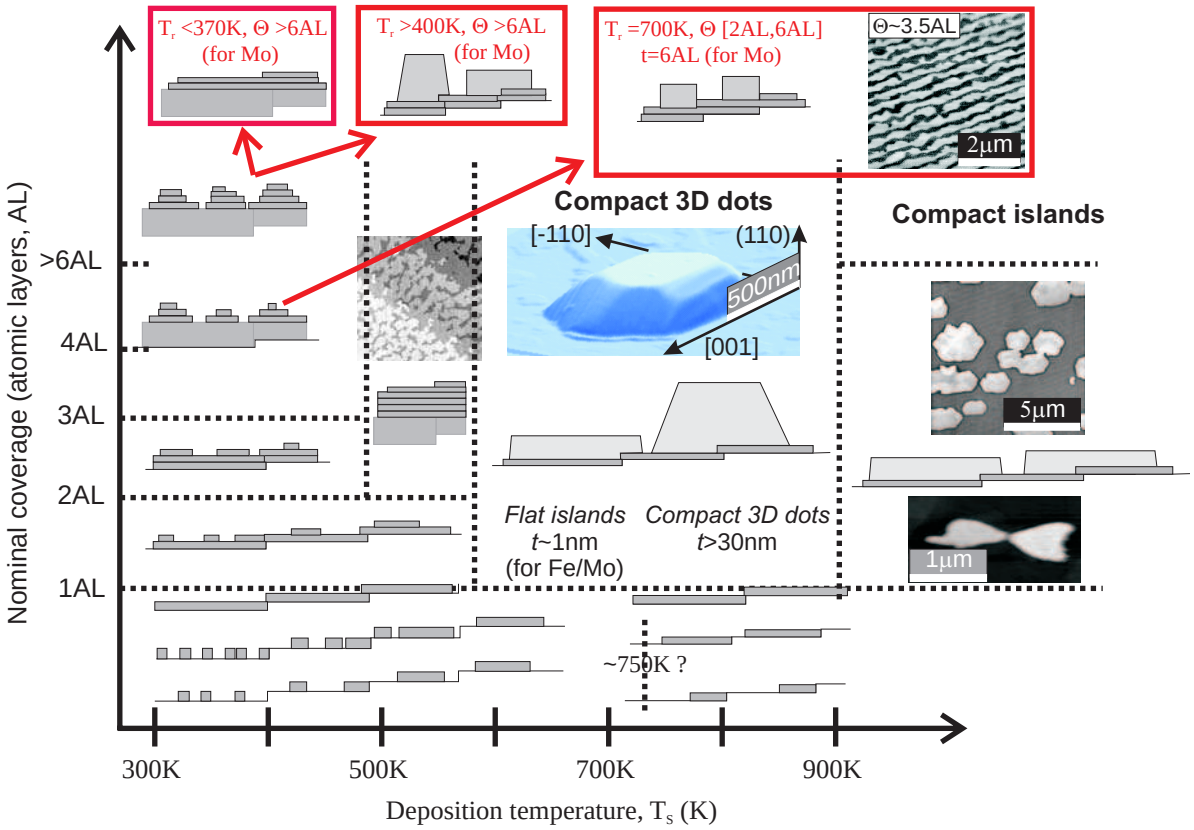

Figure 9. Schematic overview of growth modes of Fe on Mo(110) and W(110) surfaces, as a function of temperature of deposition and amount of Fe deposited. The output of annealing is displayed in rectangles. The growth modes for which we reported the first contribution are illustrated with a picture

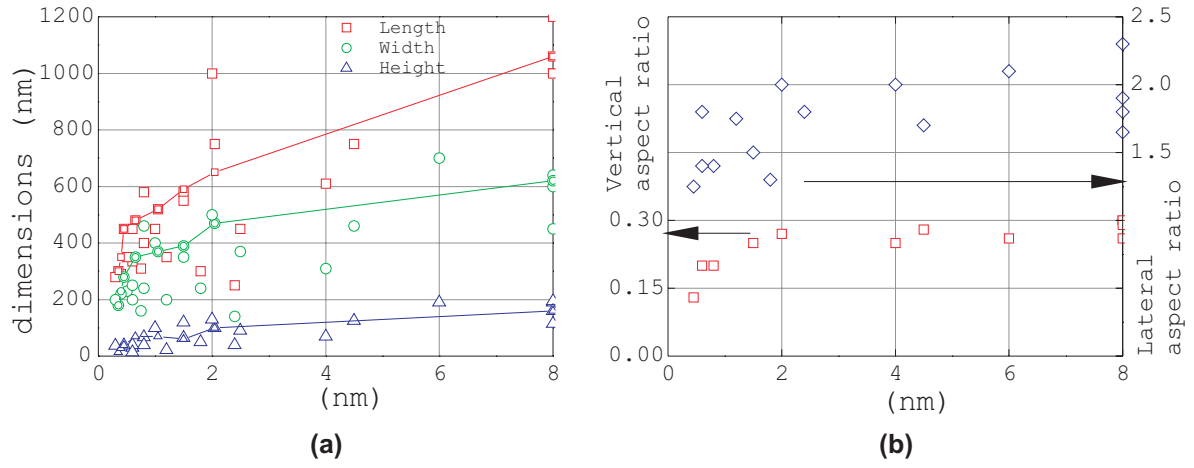

Figure 10. (a) Distribution and increase of the dimensions of compact dots for a series of samples grown at 450 °C, versus nominal thickness Θ. The full lines stand for one selected sample (b) Vertical (squares) and lateral (diamonds) aspect ratio depending on growth temperature.

patterns, much more reliably than with AFM were tip shading effects may arise for such steep slopes. The sharpness of the streaks suggests the smoothness at the atomic scale of the facets. The values of the angles of the facets are analyzed quantitatively in the following paragraph. On Figure 11 notice also the doublets of horizontal streaks, revealing the in-plane lattice parameters of both the substrate and Fe, arising from pseudomorphic areas and top facets of Fe islands, respectively. The doublets are better seen for Fe/W(110) (Figure 11d-f), where it is also clear that the intercept of the tilted streaks occurs on the horizontal streaks associated with Fe, as expected. XRD was performed in the $\theta - 2\theta$ geometry, showing that the lattice parameter of Fe in the dots equals that of bulk within better than 0.1 %. The crystalline coherence length, extracted from the analysis of the peak width using the Scherrer formula, equals the mean thickness of the dots. Owing first to the size distribution between dots, second to the distribution of local heights in each dot resulting from the tilted facets, this peak does no display side oscillations like for smooth films in Figure 4.

4.2. Wulff-Kaishev construction for Fe(110) dots

In the view of the above topographic and structural data, self-assembled Fe(110) dots can be considered to be elastically relaxed single crystals. The shape of such crystals at equilibrium on a supporting surface is described by the Wulff-Kaishev construction (Figure 13a):

$$\frac{\gamma_i}{h_i} = \frac{(\gamma_{\rm int} - \gamma_{\rm S})}{h_{\rm int}} = \text{Constant} \qquad (1)$$

where γ_i is the free energy of facets i of a given family of crystallographic planes of the material, $\gamma_{\rm S}$ is that of the free surface of the substrate, and $\gamma_{\rm int}$ is the interfacial free energy[54]. From the calculated surface energies[3], the free surfaces of a free-standing Fe crystal are expected to be mainly of type {110} and {100}, with secondary {211} and {310} facets. RHEED is consistent in revealing these four types of facets, plus {332} along the electron azimuth $< 1 - 10 >$ (Figure 11). Notice however that not all dots display facets other than {001} and {110}. Finally, sharp edges are scarcely observed by AFM. It is not clear whether this stems from the rounded shape of the tip at the scale of a few tens of nanometers, or whether edges are really rounded.

The schematic shape of both types of facetted crystals are shown in Figure 14. For comparison notice in Figure 11 that for $[1 - 10]$ and $[1 - 11]$ azimuths facets with the highest angle arise for Fe/Mo however not for Fe/W. This is explained by the fact that Fe/W crystals are flatter than Fe/Mo crystals so that steep facets are not involved, see next paragraph where the aspect ratios of the dots are analyzed quantitatively. For this analysis we introduce two parameters to characterize the islands: the lateral aspect ratio $r = L/w$ and the vertical aspect ratio $\eta = h/w$ where L, w and h are respectively the base full length, the base full width and the height (Figure 13b). These aspect ratios can be derived from Eq. (1), see Appendix I. The calculated variation of r and η versus $\gamma_{\rm int}$ are shown on Figure 15, assuming $\gamma_{\rm S} = \gamma_{\{110\}}$, see the discussion at the end of this

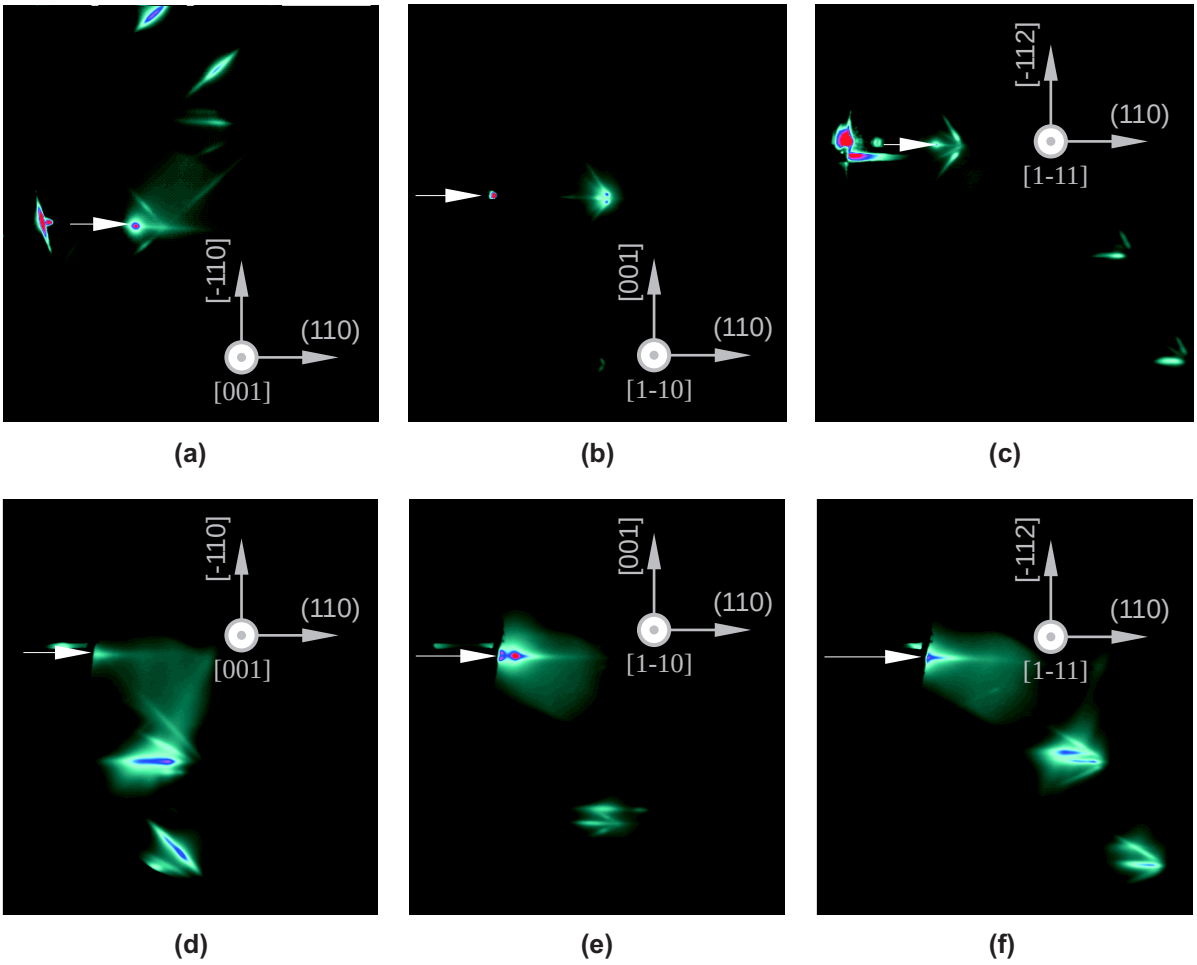

Figure 11. RHEED patterns of compact Fe(110) dots deposited on (a-c) Mo(110) and (d-f) W(110). The sample lies on the left of the patterns, with the mean surface vertical. The azimuths are (a,d) [001], (b,e) [1−10], (c,f) [1−11]. The plane of incidence is indicated with a white arrow pointing on the reflected beam. The sample is rotated a few degrees off these azimuths for all images, because this allows to better evidence the tilted streaks arising from facets. The facets evidenced are of type (a) {200} and weaker {310} (b) {112} and weaker {332} (c) {110} and weaker {211} (d) {200} and {310} (e) {332} (f) {420} (see Appendix 2).

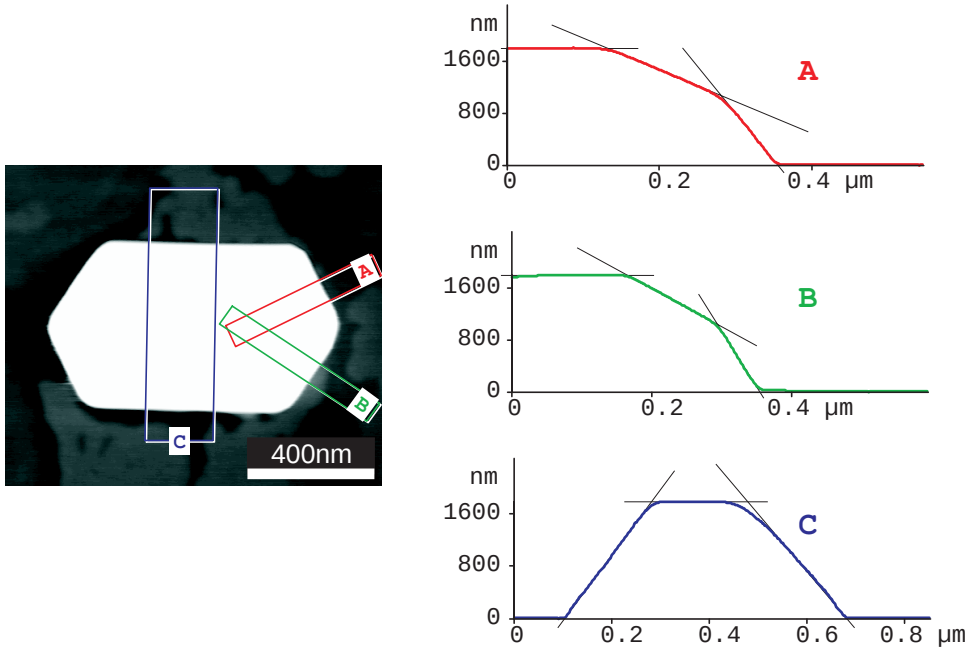

Figure 12. Experimental cross-sections averaged laterally, performed on the dot shown in Figure 8b, labelled A, B, C on the AFM picture. Thin straight lines highlight the facets on the cross-sections.

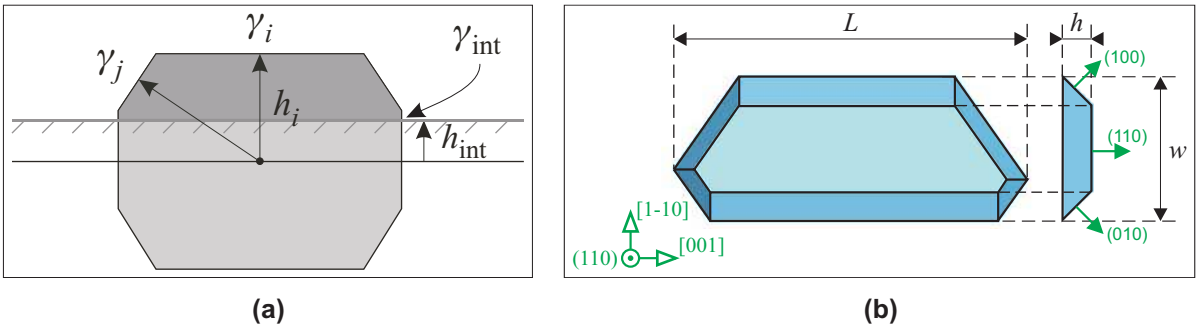

Figure 13. (a) Notations used for the Wulff-Kaishev theorem. The dashed surface stands for the supporting surface and the darker part of the crystal is the supported crystal. (b) Definition of the full width w, height h and full length L, which can also be defined if the dot does not display symmetric facets, as illustrated here.

section. The variation of η does not depend on the number of facets considered excepted for very thin dots where {310} facets come into play (see Figure 14). On the reverse for any thickness the length of the dot is reduced upon the consideration of additional facets, so that not all curves for r are superimposed.

4.3. Experimental determination of interfacial energies

The size and aspect ratios of dots on a given sample are distributed, see Figure 8. The mean experimental values of r and η are nearly independent on growth temperature (not

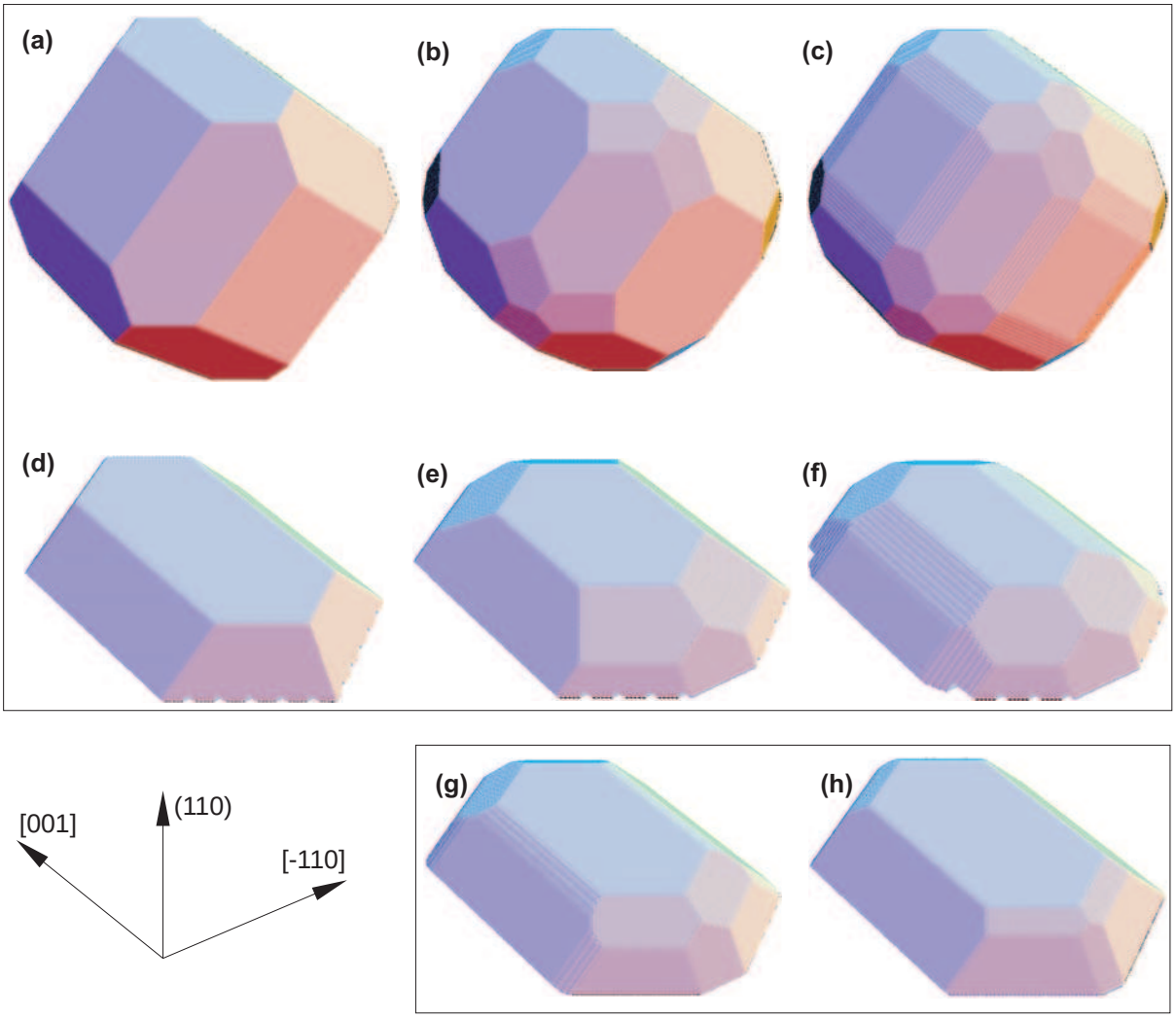

Figure 14. Wulff (a-c) and Wulff-Kaishev (d-h) constructions. (a-f) are drawn based on the values of surface energy computed by Vitos[3]: $\gamma_{\{110\}} = 2.430\,\mathrm{J/m^2}$; $\gamma_{\{001\}} = 2.222\,\mathrm{J/m^2}$; $\gamma_{\{211\}} = 2.589\,\mathrm{J/m^2}$; $\gamma_{\{310\}} = 2.393\,\mathrm{J/m^2}$. For (g) and (h) $\gamma_{\{110\}}$, $\gamma_{\{001\}}$ and γ_{int} have been reduced by 2.5 % and 5 %, respectively. (d-h) are drawn based on the interfacial energy determined experimentally: $\gamma_{\mathrm{int}} = 0.65\,\mathrm{J/m^2}$. The facets taken into account are {001} and {110} in (a,d), adding {211} in (b,e) and {310} in (c,f-h). {332} facets are not shown because their energy was not reported by Vitos, although these facets are evidenced by RHEED in the experiments (Figure 8).

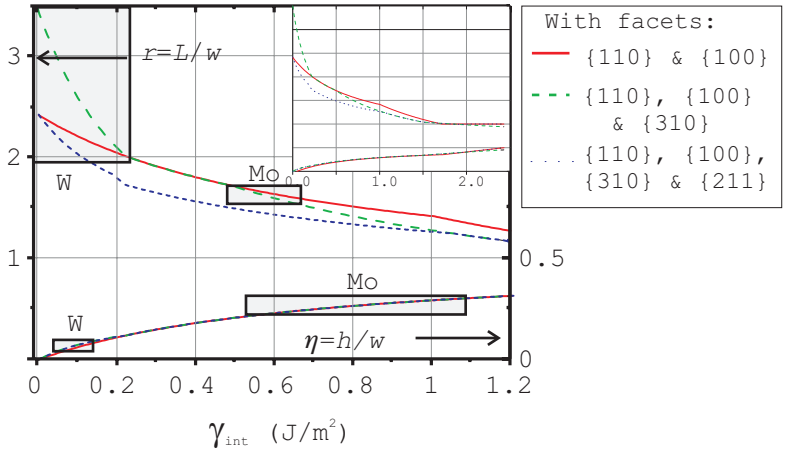

Figure 15. Lateral $r = L/w$ and vertical $\eta = h/l$ aspect ratios of supported Fe(110) dots depending on the interfacial energy $\gamma_{\rm int}$. The calculations were made considering two, three and four types of facets, and assuming $\gamma_{\rm S} = \gamma_{\{110\}}$ (see Appendix I). The vertical size of the rectangles stands for the spread of experimental aspect ratios observed for Fe/W (left) and Fe/Mo (right).

shown in this manuscript) and nominal thickness (Figure 10), as expected for an equilibrium situation resulting solely from the minimization of surface energy, with a vanishing elastic energy. We find $\eta \simeq 0.25$ and $r \simeq 1.6$ for Fe/Mo, and $\eta \simeq 0.1$ and $r \simeq 2.7$ for Fe/W. These values and their experimental distribution are reported on Figure 15 on the y axis, defining segments. The calculated curves of aspect ratios were used to convert these y-segments in segments along the x axis, defining the rectangles shown in the figure. This determines the range of interfacial energy values compatible with the observations. The relevance of the Wulff-Kaishev construction here is indicated by the overlap of the range of interfacial energies compatible with both the observed lateral and vertical aspect ratios. We deduce $\gamma_{\rm int,Mo} = 0.65 \pm 0.15\,{\rm J.m^{-2}}$ and $\gamma_{\rm int,W} = 0.10 \pm 0.05\,{\rm J.m^{-2}}$. The most probable values were derived based mostly on the value of η. Indeed, first the experimental distribution is found to be larger for r than for η, second the mean value of r was found to vary slightly more then during growth than that of η (Figure 10b). The experimental mean values for r and η have also been measured for combinations of buffer layer and pseudomorphic interfacial layers, *i.e.* Mo/W and W/Mo. It was found that $\gamma_{\rm int}$ is related to the chemical nature of the interface or interfacial layer, not on the in-plane lattice parameter imposed by the underlaying buffer layer. These facts are discussed later. In the future these studies should be extended to CGL buffer with Mo or W interfacial layers, so that the contribution of dislocations and elastic energy on effective interfacial energies is derived.

4.4. Limits of the temperature range for the growth of compact dots

The in-plane shape of the dots becomes more and more irregular when the growth temperature is reduced below $\approx 350\,^{\circ}$C, and the tilted facets tend to disappear. At

the opposite range, when the growth temperature is raised above $\approx 500\,^{\circ}\mathrm{C}$ the tilted facets are still well defined, but the aspect ratios become more and more distributed. The distribution of η broadens less than that of r. Thus, the optimum range of temperatures for growing faceted dots with a moderate distribution of aspect ratios is $350\,^{\circ}\mathrm{C} - 500\,^{\circ}\mathrm{C}$. It will be shown in sec. 5 for Fe/Mo that at still higher temperatures the SK growth is initiated with flat dots and not with compact dots.

4.5. Changes of shape induced by surfactant-mediated growth

Surfactants are used in epitaxial growth to promote a layer-by-layer growth mode like with Pb with Co/Cu(111)[58] or O for Fe(001)[59]. Kinetic effects are often identified as the leading effect promoting layer-by-layer growth[60], by lowering diffusion energies. A side effect is the lowering of surface energies when surfactants are present. The ratio of the different surface energies might be also changed, which should a modification of the shape of crystals.

We have observed a surfactant effect of Sm on Fe(110) dots. Upon deposition from a $SmFe_2$ compound target, we have observed in a narrow range of temperatures around $450\,^{\circ}\mathrm{C}$ the formation of hut-shaped dots (Figure 16a)[61]. XRD revealed that the dots are made of pure Fe relaxed to the bulk lattice parameter with no indication of Sm or any SmFe compounds. This can be explained by the low evaporation temperature of Sm under UHV, $\approx 200\,^{\circ}\mathrm{C}$, so that Sm re-evaporates from the surface and does not contribute to the formation of SmFe compounds, for which the present temperatures are too low. Auger spectra revealed that a weak amount of Sm remains at the surface, probably one atomic layer, that significantly lowers the surface energies of Fe and therefore whose evaporation is hindered[62]. These hut-shaped dots were similarly obtained after the deposition of pure Fe on ~ 1 AL Sm on Mo(110) at $475\,^{\circ}\mathrm{C}$ (Figure 16b), supporting the aforementioned growth mechanism using a $SmFe_2$ target and confirming the surfactant effect of Sm.

It is obvious that the surface energies of the various bcc-Fe facets are not decreased in a proportional way, as the huts are elongated along $[1\bar{1}0]$ and display $\{111\}$ facets on the sides and $\{001\}$ facets at both ends. No $\{110\}$ facets are visible . A naïve explanation why $\{111\}$ facets are favored to $\{110\}$ come from hexagonal symmetry of both Mo$\{111\}$ and Sm $\{0001\}$, and also the lattice mismatch being smaller for Sm(0001)/Mo(111) than for Sm(0001)/Mo(110), respectively $12\,\%$ versus $15\,\%$. The real picture is more complicated as the valence of Sm depends sensitively on strain and on the number of ALs deposited[62, 63, 64, 65].

Let us add a word about surface contamination by residual gases. In the rare cases where the level of vacuum was poor during deposition, *i.e.* typically 1×10^{-9} Torr, the shape of the dots was altered: elongated dots were formed, with their height significantly increased at both ends in a shape of dome (Figure 16c). As these domes remain located at the end of the dots, whose length increases during the course of growth, it is likely that they move along the dot while growth proceeds. The composition of the surface

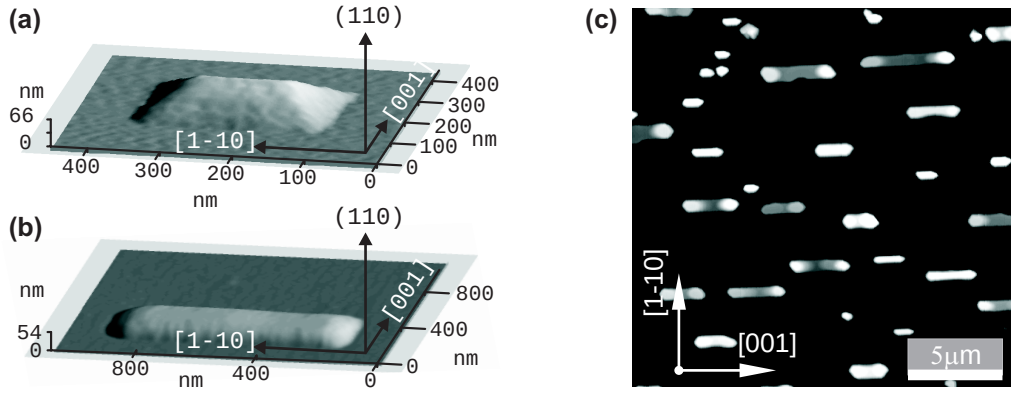

Figure 16. AFM images of an Fe(110) dot obtained (a) upon co-deposition of Fe and Sm at 450 °C (b) upon deposition at 475 °C of Fe on 1 AL Sm/Mo(110) (b) $20 \times 20\,\mu$m AFM image of Fe(110) dots deposited under poor vacuum ($\sim 1 \times 10^{-9}$ Torr).

contaminants has not been analyzed with AES.

4.6. Discussion

This discussion mainly considers the case of Fe(110) dots without surfactants. Let us first stress two points. First in our approach $\gamma_{\rm int}$ is a phenomenological value that takes into account both the chemical hybridization at the interface, and the elastic energy of the array of interfacial dislocations. This view is valid as soon as one considers islands that are significantly higher than the lateral distance between dislocations, so that the resulting strain field is averaged out in most of the island, except close to the interface. Second, the chemical part of $\gamma_{\rm int}$ shall not be interpreted as the wetting energy of Fe on either W or Mo, but as the wetting energy of Fe on either Fe(1 AL)/W or Fe(1 AL)/Mo. Indeed, the question is whether the Fe atoms will form a smooth film, or self-assemble in islands, *above* the wetting AL. Notice that this explains why surfactants like Sm are not efficient in suppressing the SK growth of dislocated dots: both the surface energy of Fe and that of the 1AL-covered substrate are reduced by the surfactant.

Let us now discuss the values determined for $\gamma_{\rm int}$ from the mean aspect ratio of the dots. We first discuss the soundness of our analysis, which is based on the numerical values of surface energy computed by Vitos *et al.* [3]. The AFM views in Figure 8(b,d) are in reasonable agreement with the theoretical picture of Figure 14d-f, which shows that the computed values of surface energy are rather accurate. However a statistical analysis of the experimental dots with AFM however reveals several details. The facets other than {001} and {110} are of smaller extent in the experiments, especially concerning {310}. Figure 14g-h show the shape of dots when $\gamma_{\{110\}}$, $\gamma_{\{001\}}$ and $\gamma_{\rm int}$ are all decreased by 2.5 % and 5 %, respectively. Theses shapes fit better the experiments. Thus, the surface energy of the facets of higher Miller index might have been underestimated in relative value by a few percent in the computation. More precise values cannot be extracted from our data because of the distribution of shape from one

dot to another. For instance, not all dots display the additional facets. Also {211} facets at the base of the dots (at the end of the arrows) are more rarely found than those around the {110} top. These uncertainties over the values of surface energy might contribute to the only partial overlap of the ranges of interfacial energies compatible with the experimental observations of η and r, see Figure 15

Let us now discuss the values derived for $\gamma_{\rm int}$. $\gamma_{\rm int}$ was found to depend on the interfacial layer and not on the underlying buffer layer, which is not surprising. Indeed W and Mo have similar lattice parameters, 3.165 Å and 3.147 Å, respectively. Thus a similar lattice misfit with Fe is expected, inducing a similar density of the interfacial dislocations network, and thus a similar areal density of elastic energy. Concerning the dependence on the interfacial layer, two phenomena may play a role. First the strain field of the interfacial dislocations extends down mostly into this layer, not in the underlying buffer layer. Thus, from the higher elastic constants of W over Mo one would expect $\gamma_{\rm int,W} > \gamma_{\rm int,Mo}$. As the reverse relationship is observed the second effect must therefore be dominant and with an opposite trend: the surface band structure of one atomic layer of Fe has not recovered that of the surface of a bulk Fe crystal, and is still influenced by the underlying material. More specifically, Eq. (1) shows that what matters is not solely $\gamma_{\rm int}$, but $\gamma_{\rm int} - \gamma_{\rm S}$, S being here respective to the wetting monolayer. We already mentioned that the plots of Figure 15 has been computed assuming assuming $\gamma_{\rm S} = \gamma_{\{110\}}$. This was assumed because no figure is known for the surface energy of the monolayer of Fe(110). As a consequence it is not possible to disentangle $\gamma_{\rm int}$ from $\gamma_{\rm S}$. A point of view would be to conclude that Fe(1 AL)/W has a higher surface energy than Fe(1 AL)/Mo, which seems reasonable as the same relationship holds for the bulk materials: $\gamma_{\rm W} \sim 4.0\,{\rm J/m^2}$ and $\gamma_{\rm Mo} \sim 3.4\,{\rm J/m^2}$.

So far we have neglected a potential residual strain in the dots. The residual strain is less than 0.1% as probed by XRD, which corresponds to a stored elastic energy $E_{\rm elas}/V_0^{2/3} = 0.2\,{\rm J/m^2}$. Only a small fraction of $E_{\rm elas}$ may be gained by changing the island shape, say approximately at most 10-20% due to a moderate vertical aspect ratio, which amounts to about$0.04\,{\rm J/m^2}$. As the equilibrium dot shape results from the interplay of the elastic energy and the surface/interface energy, let us estimate how a surface/interface energy excess of $0.04\,{\rm J/m^2}$ would influence the shape of the dot. Figure 17 shows the total surface/interface energy per unit of the island volume (more precisely the scalable quantity $E_{\rm s}/V_0^{2/3}$) as a function of η and r, plotted for $\gamma_{\rm int} = 0.5\,{\rm J/m^2}$. The energy minimum is obtained for $r = 1.7$ and $\eta = 0.2$ which corresponds to $E_{\rm s}/V_0^{2/3} = 4.33\,{\rm J/m^2}$. An excess of $0.04\,{\rm J/m^2}$ in the surface energy would correspond to a variation in the aspect ratios of $\Delta r = \pm 0.4$ or $\Delta\eta = \pm 0.05$. These deviations from the calculated equilibrium shape are small and comparable to the experimental distributions. Thus the effect of residual elastic strain can not be distinguished, at least directly. However strain effects might also contribute for the only partial overlap of the ranges of interfacial energies compatible with the experimental observations of η and r, see Figure 15.

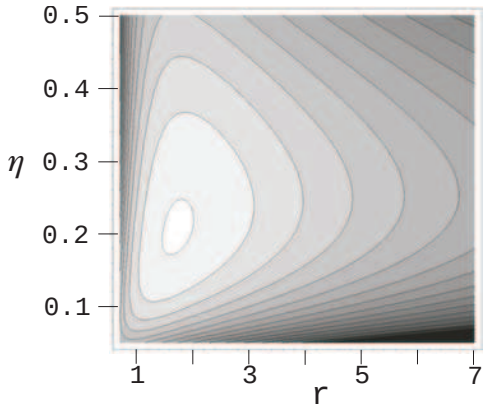

Figure 17. Total surface/interface energy of a Fe(110) dot calculated with $\gamma_{\rm int} = 0.5\,{\rm J/m^2}$. The minimum of energy is reached for $r = 1.7$ and $\eta = 0.2$ which corresponds to $E_{\rm s}/V_0^{2/3} = 4.33\,{\rm J/m^2}$. The energy difference between lines of equal energy is $200\,{\rm mJ/m^2}$.

5. Flat islands and stripes

In this section we report results pertaining to flat nanostructures that arise in the bimodal growth mode (Figure 8a). Contrary to the case of compact islands that grow homothetically in the course of deposition–see previous section, the height of the flat nanostructures remains essentially constant during growth, while only their laterals dimensions increase. The occurrence of one or several such heights, constant during growth and therefore presumed to be stable or metastable, has been reported for several systems: Ag/GaAs(110)[66], Ag/Si(111)[70, 71], Ag/Fe(001)[72], Pb/Si(111)[67, 68, 69], Pb/Cu(111)[73]. These heights are sometimes called magic height, because their occurrence is unexpected within the scheme of classical growth modes, either Volmer-Weber (VW), Franck van den Merwe (FM) or Stranski-Krastanov (SK). In the following we will refer to these nanostructures as *preferred* height instead of *magic* height. We first give evidence for the bimodal SK growth mode for Fe(110), then demonstrate the metastability of the preferred height and discuss possible physical phenomena that can give rise to such effects. Finally we show how the occurrence of a preferred height can be used to fabricate unusual self-organized systems, namely thick stripes by step decoration, and nano-ties.

5.1. Bimodal SK growth

Most of our experiments were performed on Mo(110) or Mo-covered W(110). We evidenced the bimodal growth of Fe(110) in the approximate range of temperature $250 \sim 500\,^\circ$C (the bounds were not determined accurately), as shown in Figure 8a. Apart from the compact islands appearing as bright dots in this figure, and the wetting layer appearing as the darkest background with an array of parallel monoatomic steps, flat islands with a large ratio of lateral size over height are observed. Important to

notice is that the height of these islands essentially does not vary during growth. The further deposition of material only contributes to increase their area through lateral growth. For deposition on pure Mo buffer layers the distribution of heights is narrow: $h = 1.2 \pm 0.2$ nm above the wetting AL, *i.e.* implying a mean total height of 7 AL above Mo. Details about the size and density of these islands can be found in Ref. [35]. Their shape depends on the growth temperature, see Figs. 8a, 18, 24. For the lowest range of temperatures for the bimodal SK growth, *i.e.* around 400 °C, the islands seem to grow in the direction perpendicular to the steps of the substrate, with a shape influenced by single atomic steps in a saw-tooth-like manner, see Figure 8. At higher temperatures the islands have a tendency to display a hexagonal shape elongated parallel to [001], be it while the growth remains bimodal (not shown here) or when only wedged islands grow at very high temperature (Figure 18). In all cases notice that the top of these nanostructures is not perfectly flat, but displays a weak density of single atomic steps to compensate for the residual miscut, thereby allowing to keep a mean constant thickness over lateral distances over micronmeters (Figure 18). This confirms the stability of the preferred height. If it were not stable, these steps would flow over the top during growth, ending up in wedged islands. This phenomenon is observed in the first stages of growth of Fe/Mo(110)[16] and Fe/W(110)[11], below the constant preferred height. When no preferred height exists, like for Au/Mo(110), these islands grow endlessly laterally in the downward step direction (Figure 19). Beyond the case of Mo(110), the formation of wedged islands is a common phenomenon on surfaces displaying atomic steps[11, 67, 74] and the microscopic phenomena explaining the growth or diffusion along the downward direction have been unveiled by monitoring growth *in situ* [75]. Coming back to Fe(110), deposition on W is qualitatively similar to the case of Mo, however with a higher preferred height and a broader distribution, $t = 6 \pm 2$ nm. Notice also that the density (resp. the lateral size) of these islands is lower (resp. larger) than for deposition on Mo.

5.2. Evidence for the metastability of the preferred height

The occurrence of flat islands whose height does not vary during growth and is independent from the deposition temperature, suggests that their exists a stable or metastable height for Fe/bcc(110) systems. It is the purpose of this sub-section to support this assumption. The possible physical driving forces for the occurrence of such a preferred height will be discussed in sub-section 5.6.

Fe was deposited at RT on Mo(110) with a nominal thickness $\Theta = 0 - 2$ nm varied as a wedge over the entire length of the substrate. The growth resulted in a roof-like rough surface[21], as first reported in Ref.[20], and similar to the rough surfaces of moderate-temperature-deposited Mo and W layers reported in sec. 2 (Figure 2). Upon annealing at 450 °C this rough film unwets Mo, and thus Fe nanostructures are formed (Figure 20). For $\Theta \leq 7$ AL the nanostructures have all the same uniform height $t = 1.2 \pm 0.2$ nm. The area covered by the nanostructures increases as a function of

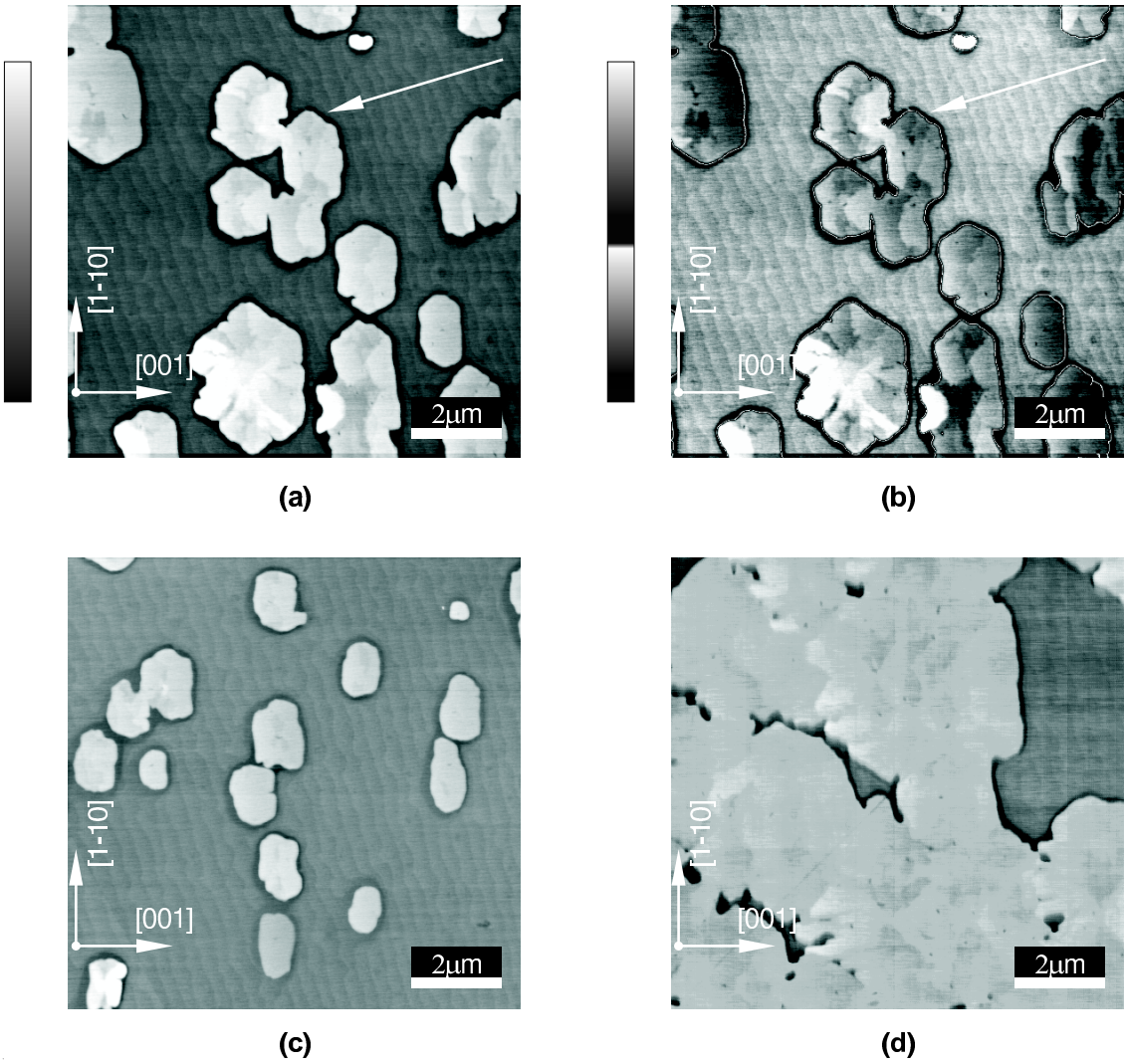

Figure 18. Flat Fe(110) islands resulting from the deposition at 800 °C on Mo, seen on $10 \times 10\,\mu$m AFM images. The white arrows indicate the downward direction of the array of mono atomic steps of the buffer layer (a) $\Theta = 0.5$ nm normal scale (grey scale shown on the left) (b) same picture with a split scale (see second scale bar) to achieve a significant contrast for both the background and the top of the islands. (c) $\Theta = 0.25$ nm (d) $\Theta = 1.25$ nm

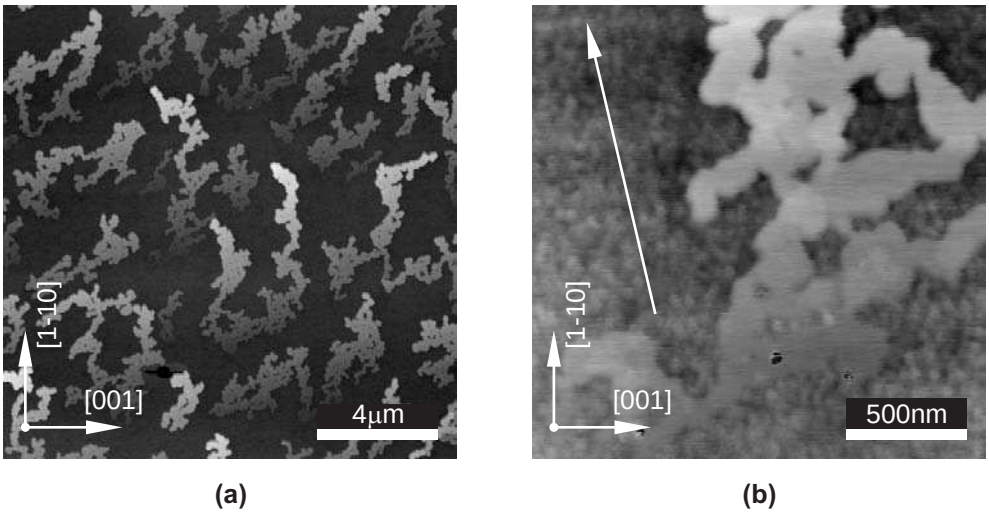

Figure 19. AFM images of Au($\Theta = 7.5$ nm)/Mo(110) upon deposition at 600 °C. The white arrow in (b) indicates the downward direction of the array of mono atomic steps of the buffer layer.

nominal thickness, until a nearly continuous layer 7 AL-high is formed. We hereby confirm that the occurrence of a preferred height gives the mean to achieve very smooth continuous films for SK systems. From this experiment we also conclude that 7 AL is a highly preferred height for Fe/Mo(110). For $\Theta > 7$ AL compact islands of height much larger than 7 AL nucleate, and for most of them grow at the expense of the continuous film: channels have formed in this film, an effect which therefore seems to result from the diffusion of atoms towards the compact islands. From the latter observation we finally conclude that 7 AL is a *metastable* thickness, *i.e.* it is favorable against other numbers of ALs in the range of small thickness, however it is unstable with respect to much thicker structures.

The experiment of room temperature deposition followed by annealing has not been conducted for Fe/W(110). However, we will see that the experiment on self-organized stripes, reported hereafter, leads us to the conclusion that a metastable thickness also exists for this system.

5.3. Fabrication of wires self-organized along steps

In this sub-section we show how the (meta)stability of layers with a preferred height can be used to produce self-organized thick stripes decorating the array of mono-atomic steps of buffer layers. By *thick* we mean much higher than one or two atomic layer(s), which are the heights usually reported in the literature, for self-organized stripes fabricated by step decoration.

On Figure 20a-b the nanostructures display a preferential alignment along one single well-defined direction. This direction is not a low Miller index crystalline axis, but is related to the underlying array of mono-atomic steps of the buffer layer. Indeed,

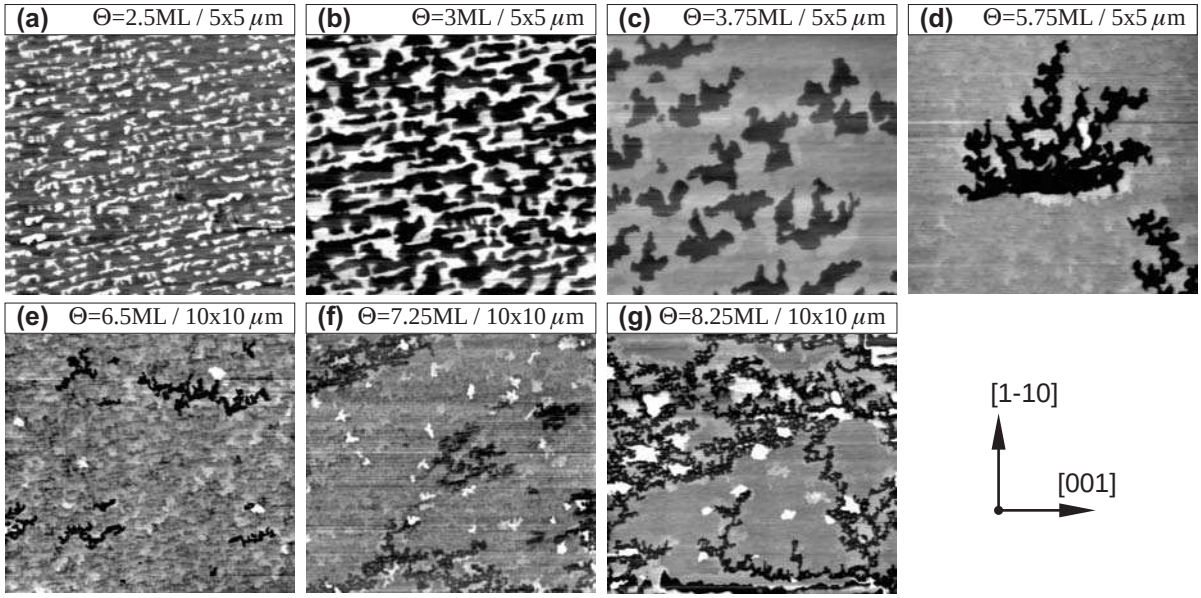

Figure 20. AFM images of Fe deposited on Mo(110) at room temperature, followed by annealing at 450 °C, for several nominal thicknesses Θ. Notice the different scale used for the two rows.

comparison with AFM images of the raw buffer layers reveals that these stripe-like features display the same orientation, and the same period across the stripes, as that of the array of steps on the Mo surface. These steps are thus expected to play a role in the unwetting process. The tendency to form stripes can be enhanced if deposition is performed slightly above room temperature, in the range around $150 - 200\,^{\circ}$C, followed again by annealing around 450 °C, the exact value of the latter temperature being not crucial in the process (Figure 22). The reason for improvement is revealed by STM images taken before and after annealing (Figure 21)[39]. Growth at 200 °C proceeds layer-by-layer. However beyond 2 AL grooves appear at the surface of the film, with the same orientation and spacing as the array of mono-atomic step of Mo. It is likely that the grooves appear above these buried mono-atomic steps, driven by the strain resulting from the misfit of height between (110) atomic layers of Mo and Fe, 2.23 Å and 2.03 Å, respectively. The tendency to have grooves close to steps of the buffer layer could be seen on a Fig.1b of Ref.[16] for Fe grown on Mo at RT. The grooves then probably act as nucleation sites for unwetting during the annealing, yielding stripes. Notice that the straighter side of the stripes lies along the ascending step, probably because the strain acts as a barrier. It has not been attempted to systematically investigate annealing or other procedures to improve the free side of the stripes, which is much rougher on this image. We however stress that neither deposition nor annealing temperatures are critical parameters for getting stripes. Notice that such stripes can be fabricated in any orientation away from [001] to $[1\bar{1}0]$ (Figure 22), which definitely shows that there is no correlation between their orientation and crystallographic directions. Notice that in our early reports non-connected Fe/Mo(110) stripes, of irregular shape and height, were

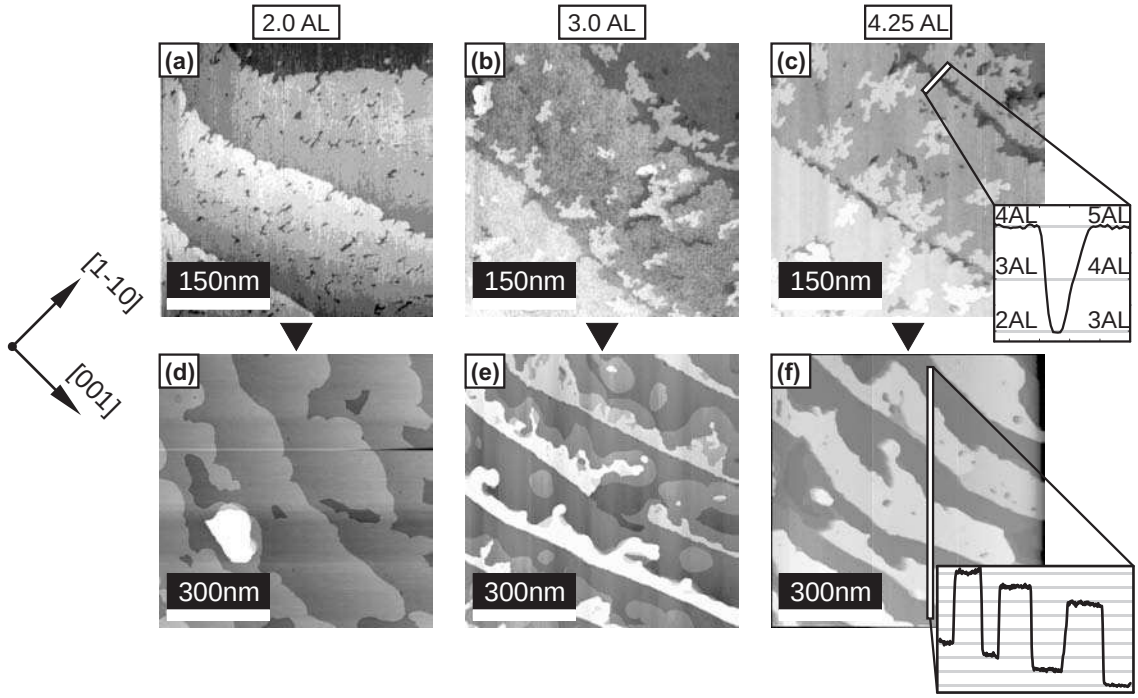

Figure 21. STM images of Fe/Mo(110) (a-c) after deposition at 200 °C and (d-f) after annealing at 450 °C.

produced by deposition at 250 °C followed by annealing at 450 °C[37].

Figure 23 shows Fe/W(110) and Fe/Mo/W(110) nanostructures obtained following the same procedure as for Mo: deposition at 200 °C followed by annealing at 450 °C. Stripes are again formed, however with increased height, centered around 5.5 nm. As in the case of Mo, this suggests that the stripes can be formed thanks to the occurrence

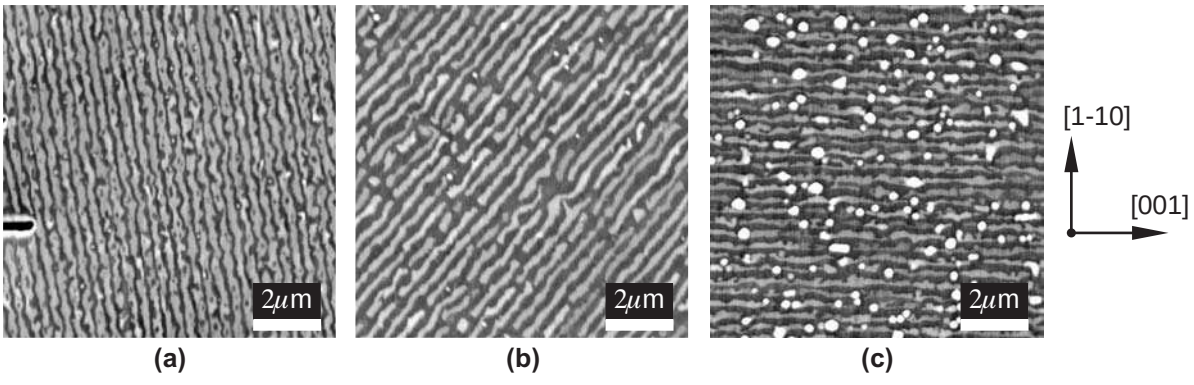

Figure 22. AFM images of stripes formed by deposition of Fe on Mo(110) at 200 °C, followed by annealing at 450 °C. The direction of the stripes follows that of the array of atomic steps of the buffer layer, itself in turn dictated by the miscut of the substrate. In (c) a non-optimized growth procedure (slightly too high temperature) is responsible for the occurrence of somewhat thicker dots in the course of the stripes.

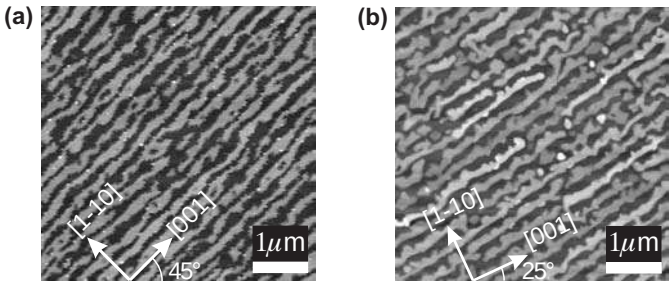

Figure 23. *ex situ* AFM images of (a) Fe/W(110) and (b) Fe/Mo/W(110) stripes obtained by deposition at 200 °C followed by annealing at 450 °C.

of a metastable height. However the height distribution is larger, and varies slightly with the amount of material deposited. This suggest that the energy minimum for the preferred height is shallower for Fe/W(110) than for Fe/Mo(110). It is also evident that the quality of the stripes is higher for Fe/Mo than for Fe/W. This may stem from the fact that unwetting starts from a film much thicker for the latter. The quality of the wires could presumably be improved by a detailed investigation of the shape and depth of grooves formed at the steps during deposition at 200 °C, to better assist the unwetting process.

The new process described here, of nanometers-thick stripe formation, is an advancement in self-organized systems. Indeed the height of metallic stripes and islands produced by mono-atomic step-decoration was until now limited to one or two AL[24, 23, 55, 76, 77, 78]. In the field of magnetism this was a fundamental obstacle against the use of such systems for the fabrication of functional materials, as ferromagnetism was lost at RT because of the low dimensionality. This obstacle is overcome with the new process[39]. It is therefore of importance to determine whether this process is specific to Fe(110) or not. As mentioned above stable heights have been reported for a series of other systems. Besides, grooves at steps or the strong influence of steps in unwetting processes were reported for other systems like FeNi/Cu(111)[79] and Cu and Ag/Ru(0001)[75]. We also reported the influence of atomic steps of the substrate for Tb/Mo(110)[42]. As these are the two ingredients that we have identified to yield thick self-organized stripes, it is likely that the process reported here should occur for other systems.

5.4. Mono-modal growth of flat islands at very high temperature

For growth at very high temperature only flat structures form, with no more compact islands (Figure 18). For Fe/Mo(110) the distribution of heights is again monomodal, centered around 1.5 nm with however a slightly broader distribution compared to the growth at lower temperatures. Notice that the top surface of the islands tends to be flat, yielding wedge-shaped islands. Only when the islands have a very large lateral size steps of mono- or multi-atomic height are observed on the top surface, which tend to suppress

the wedge on long distances. This again is an indication of the strong stability of the preferred height for Fe/Mo(110). The statistical examination of cross-sections of the islands reveals that the height distribution, increased as compared to the case of stripes, primarily arises from the wedge effect, while the distribution of the *average* height of the islands is much narrow. Notice also the tendency of these islands to be elongated along $[1-10]$ with arrow-like ends with edges along the in-plane $\{111\}$ directions, and that no clear effect of the steps of the underlying Mo can be evidenced. We believe that the agreement with the height of stripes presented in the previous sub-section is not fortuitous. However the growth mode at very high temperature is more complex and needs to be clarified. For example, we cannot exclude that interfacial alloying between Fe and Mo is involved to some extent in the formation of these islands, as the possibility of Fe/Mo(110) alloying was reported at high temperature[2].

Finally, notice that no indication on the type of lateral facets could be obtained from RHEED in the case of mono-disperse assemblies of thin flat islands, because of the weak area of the facets. Also, beyond the close completion of a uniform film upon percolation of these islands, three-dimensional compact dots start to nucleate, with the same aspect ratios as previously reported.

5.5. Self-assembled nanobowties

With a view to understanding the growth process of islands at very high temperature we have investigated the nucleation regime (see Figure 24. Here the deposition was performed on a buffer layer of solid solution, see later). The islands then appear as being made of two main parts, separated by a constriction ever more pronounced for smaller nominal thickness. The very first stages of nucleation even seem to consist of two disconnected islands (Figure 24f) that progressively merge during subsequent growth. During the merging process one gets peculiar nanobowtie shapes consisting of two triangular very flat plateaus of height around a few nanometers, facing each other on either side of a geometrical constriction. The constriction can be very narrow (50 nm or lower) and is two dimensional, in the sense that the height is also reduced locally. Such objects might prove useful for the study of magnetic domain walls in constrictions.

The surface mobility of metals is so high at these temperatures that the atomistic processes underlying the nucleation of nanobowties is certainly complex, and remains at the moment unclear. Notice for instance the depletions occurring around the nanobowties (Figure 18). The depth of these depletions is larger than one atomic layer, so that beyond the wetting layer of Fe this suggests material transfer from the substrate. Whether this material is incorporated in the island or driven away is unknown. Such erosion effects are known to occur for other materials, provided that they are energetically favorable and the mobility of atoms is sufficient. Erosion processes are known to occur at room temperature in the favorable cases like Co/Cu(111)[80, 81, 82] or Fe/Cu(111)[55]. As the bare Mo surface already flows step-by-step by 2D evaporation at the present very high temperatures, it is clear that mobility is sufficient to account for

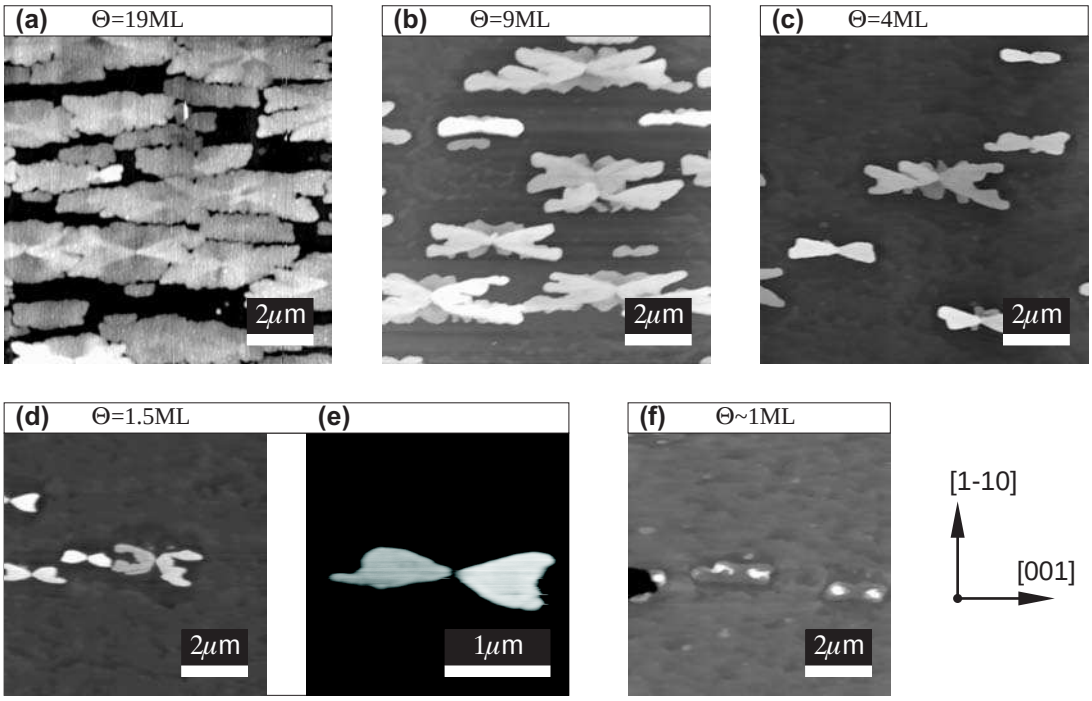

Figure 24. *ex situ* AFM images of Fe grown at 800 °C on $W/Mo_{10}W_{90}(110)$. Notice the different scale in (e).

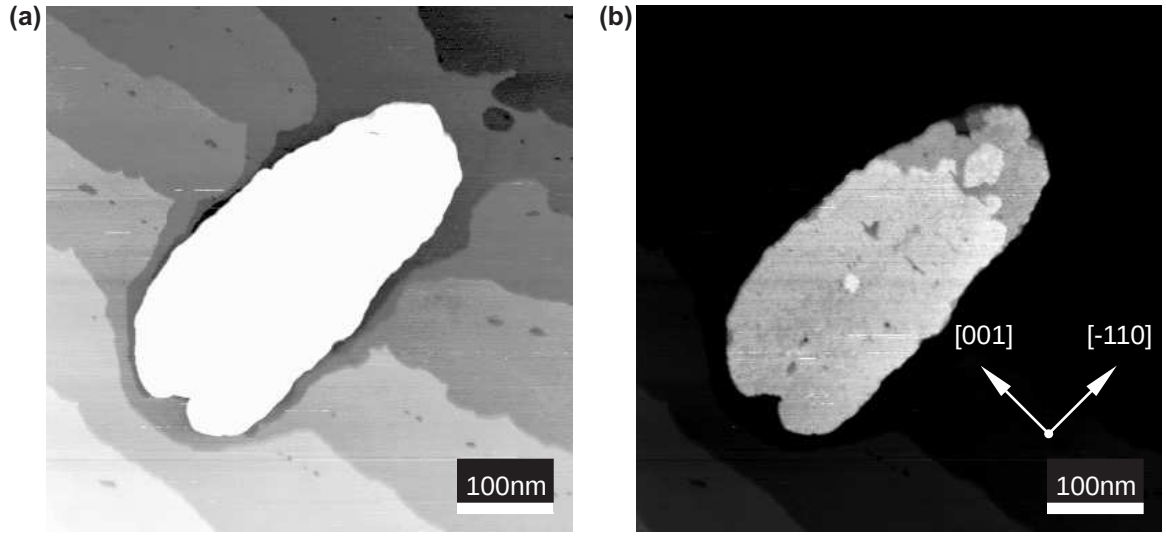

Figure 25. STM image revealing the etching process around wedge-shaped flat Fe islands grown on Mo(110) at 525 °C. A different color scale is used in (a) and (b), to highlight the steps of the buffer layer and the top of the dot, respectively

.

these effects. Notice that a depletion could already be observed around dots deposited at intermediate temperature in our experiments (Figure 25) as well as in the literature (see [32], Fig.1b). For Fe/Mo(110) the etching of substrate atoms around the dots is likely to be driven be the strain field arising from Fe, radially compressive below the dots and extensive at its outer perimeter[83]. Erosion of atoms from the substrate seems much more limited or even hindered for the case of Fe/W(110), as reported in the literature[30].

Finally, it cannot be excluded that minute amounts of contaminants, either of gaseous or solid origin, may play a role in the nucleation of nanobowties. Indeed the nucleation density is so low that the level of contamination required to influence the nucleation sites lies well below the sensitivity of Auger.

5.6. Physical origin of the preferred height

Up to now we have only described the occurrence of preferred heights. In this sub-section we propose some directions to explain this phenomenon. Let us first reject irrelevant physical phenomena, before proposing the two most appealing explanations.

First notice that the close coincidence of the height of nanostructures fabricated by deposition plus annealing on one side, and directly obtained by deposition in the bimodal SK growth mode in a broad high temperature range or in a monomodal growth mode at very high temperature as reported previously, strongly suggests that this height stands for a minimum of energy for an Fe(110) film, and does not result from kinetic effects.

Another argument to reject would be alloying at the interface, with the flat islands being made of this alloy. This is first in contradiction with the reported complete interface inertness for Fe/W(110) and very weak reactivity for Fe/Mo(110)[2]. Besides, XRD was performed on Fe/Mo and Fe/W stripes. Grazing-incidence XRD revealed in both systems the occurrence of the bulk Fe lattice parameter, with a residual tensile strain lower than 1%. Out-of-plane in-lab characterization could not be carried out on Fe/Mo stripes because the resulting peak is too broad. For Fe/W the bulk Fe lattice parameter was retrieved with a slight residual tensile strain of 0.4 %. Most importantly, in this case the out-of-plane crystallographic coherence length of the nanostructures, as determined with the Scherrer formula from the width of the peak, yielded 5.5 nm in exact agreement with height inferred from AFM. As a whole this suggests that the stripes observed by AFM and STM are made of bulk-like Fe in their entire thickness.

Still another argument to reject would be that the bimodal growth might result from size-dependant strain minimization effects. Indeed cases of bimodal growth are common for semiconductors (the so-called domes and huts[84, 85]) for SK growth modes. This effect was explained as resulting from the competition of the reduction of surface energy roughly scaling with the square power of size (the surface), versus strain energy via *elastic* deformation that roughly scales with the third power of size (the volume), thus explaining a transition as a function of size, which indeed fitted the experimental

observations. However this effect requires a large strain and still coherently-strain islands, which is not the case for Fe/cc(110) flat islands. Besides, strain is efficiently reduced only in compact islands. Here strain reduction cannot be a driving force for selecting a value for a uniform height of islands with a lateral aspect ratio over 100.

The first potential explanation remaining is a quantum size effect, which was recently definitely proven to give rise to preferred and hindered values in the distribution of heights[73]. In short, the confinement of electrons along the direction perpendicular to a layer gives rise to quantum well states (QWS). The density of energy of the layer is minimum when the occupied QWS highest in energy is far below the Fermi energy. An argument going in this direction is the tendency to observe a multimodal distribution of heights both for Fe/Mo(110) and Fe/W(110), especially in the case of annealing procedures. This can for example be evidenced by scrutinizing Figure 20 where the flat areas of preferred height are decorated with a brim of preferred height, however with a larger value. To confirm this we recently evidenced *in situ* with LEEM sudden transitions of height of Fe/W(110) islands[57]. If this explanation is correct an open question is why the values of preferred heights depend so sensitively on the buffer and capping layer, Mo or W, an effect which could not be explained in the simple model of Ref.[73].

The second potential explanation is a transition of the network of dislocations at the interface between Fe and the buffer layer, from a periodic sequence for low thickness to ideally a non-periodic sequence for large thickness. Indeed in the limit of ultrathin films one expects that a periodic arrangement of dislocations is the state of lowest energy. This can be understood as nearest-neighbor interactions dominate in the *total* energy for low thickness. To the contrary for very thick films the interface contributes very little to the total energy of the system. If the dislocation network is periodic a small residual strain remains in the entire system because the lattice parameters of the two elements are not commensurate. Then, it should be energetically favorable to reorganize the array of dislocations in a non-periodic sequence at the cost of a finite interfacial energy, as this allows to lower the strain energy in a majority part of the system. It is appealing to think that the preferred height could be the critical height for such a transition. In the case of a commensurate/incommensurate transition one expects a very rapid variation of behavior as a function of the lattice parameter of the substrate, as what counts is not directly the misfit, but the residual lateral misfit, *i.e.* the misfit between N atoms of the substrate versus $N+1$ atoms of Fe at the interface. The larger the residual misfit, the lower the critical thickness would be. Let us give figures. The misfit of Fe with Mo is 9.79 %, as defined by $\epsilon = (a_{\mathrm{Mo}} - a_{\mathrm{Fe}})/a_{\mathrm{Fe}}$, and that with W is 10.42 %. Table 1 shows the residual misfit expected for arrays of dislocations with various periods. The table shows that, assuming a positive residual misfit as is often reported, $N = 11$ and $\epsilon = +0.64\,\%$ in the case of Fe/Mo, and $N = 10$ and $\epsilon = +0.38\,\%$ in the case of Fe/W. These figures are coherent in sign and magnitude with those determined experimentally by XRD in wires organized along steps. We mentioned in sec. 4 that the compacts dots are relaxed to better than 0.1 %, which proves that the arrays of interfacial dislocations evolves at

Table 1. Residual misfit of Fe on Mo(110) and W(110) for a periodic array of dislocations, when a series of $N+1$ Fe atoms coincides with N atoms of the substrate.

N	With Mo	With W
9	-1.19 %	-0.62 %
10	-0.20 %	+0.38 %
11	+0.64 %	+1.22 %

some point. According to the above figure the elastic energy associated with the residual strain is expected to be $3-4$ times larger for Fe/Mo than for Fe/W, which would imply the reverse relationship for the critical thickness, which is the case in the experiments for the preferred height. Despite this agreement, the possible link with the preferred height remains at this point speculative until further experimental data is available. Notice that the figures of low strain given above contrast with surface XRD measurements of the strain for Fe/W(110), which conclude that a positive strain isotropic in-the-plane remains, equalling 1.22 %[15]. The discrepancy might arise from the fact that these authors studied a *continuous* film of thickness 12 AL, grown at 300 K and only slightly annealed. In this case of a continuous film the array of dislocations if completely formed in the early stages of growth, and the density of dislocations may not find a pathway to evolve. A different situation is expected for nanostructures where dislocations can enter or be expelled at the perimeter or nanostructures. Thus, a comparison of our results with those of Ref.[15] may not be done directly.

To decide what explanation is correct between quantum size effects or a commensurate to incommensurate transition will require calculations and further experiments, both of growth and of characterization. In the next paragraph we report a route that may help gathering in the future enough data to solve the matter.

5.7. Deposition on interfacial layers and solid solutions

In this paragraph we present preliminary results concerning the growth of Fe nanostructures on the composite buffer layers described in part 2.

To prove unambiguously which of the two explanations for the preferred height is correct will require analyzing the role of several parameters independently, for instance hybridization at the interface to affect quantum size effects, and lattice misfit to influence the density of interfacial dislocations. For the latter a continuous variation is desirable because a full curve provides more information than just a few points.

To vary independently the lattice parameter and the chemical nature of the supporting surface we apply the procedures reported in section 2 for the fabrication of buffer layers. Concerning the control of the interface we found the following values for critical thickness, as deduced from self-organized stripes: $t_{\mathrm{Fe/W}} \sim 5.5\,\mathrm{nm}$, $t_{\mathrm{Fe/Mo}} \sim 1.4\,\mathrm{nm}$, $t_{\mathrm{Fe/Mo/W}} \sim 6\,\mathrm{nm}$, $t_{\mathrm{Fe/W/Mo}} \sim 4.5\,\mathrm{nm}$. It is already clear that both the in-plane lattice parameter and the chemical nature of the interface, influence the metastable thickness of the stripes.

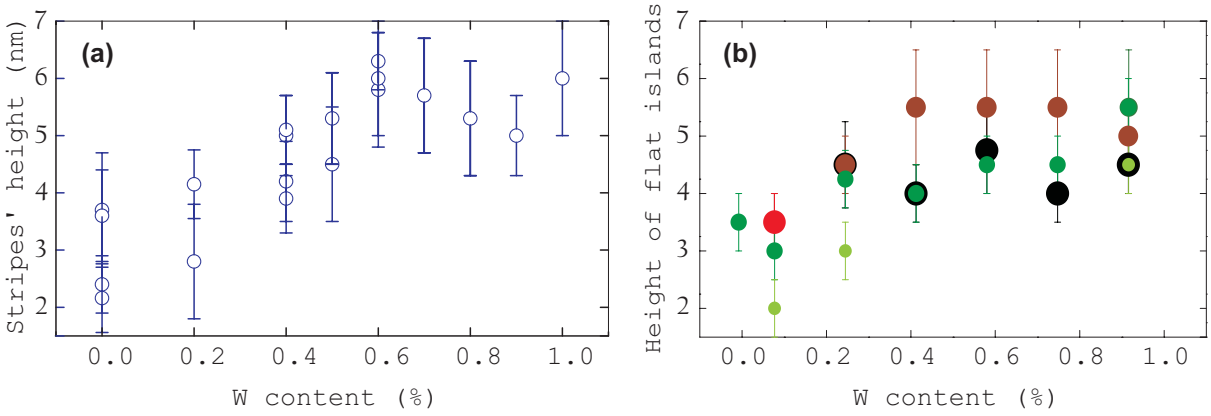

Figure 26. Height of Fe(110) nanostructures obtained upon deposition on Mo(3 AL)/W_xMo_{1-x} composite buffer layers. For both curves the error bars stand for the full width of the experimental distribution over the assembly of nanostructures. (a) Stripes decorating steps, upon deposition at 200 °C and annealing at 500 °C (b) flat islands upon deposition at 800 °C. For the latter case the distribution of height is multimodal, the height being larger for the area related to the initial stages of growth with a shape of bow tie (Figure 24). In the present figure we plot the height of the remaining part of these dots, which is flat, monomodal and does not vary significantly upon deposition. The diameter of the symbols stands for the nominal thickness Θ of Fe, ranging from zero to 4 nm. The color, constant for each Θ, is used for clarity when several symbols overlap.

Concerning the variation of lattice parameter Table 1 shows that there exists a concentration x of the solid solution W_xMo_{1-x} for which the misfit cancels out. For this concentration in principle the critical thickness should go to infinity for commensurate lattices, although in a real experiment other effects will interfere. The differential thermal expansion between Sapphire and the metals should also be taken in to account. In Figure 26 we plot the preferred height of nanostructures as a continuous function of the lattice parameter, for the interface Mo(3 AL). Figure 26a displays figures concerning stripes obtained upon deposition at moderate temperature followed by annealing. Figure 26b displays values concerning islands obtained upon deposition at very high temperature. First notice the remarkable agreement between the two curves. This suggests that the preferred height really comes from an energetic minimum rather that results from a kinetic effect, as the two fabrication procedures are very different. Besides, the height varies significantly with the lattice parameter of the buffer layer. However no clear maximum is observed, which would have been the experimental signature for a divergence expected theoretically. At this point our experiments are therefore not conclusive concerning the role of lattice parameter. Extension of these results to a variation of lattice parameter much beyond the range offered by mixtures of Mo and W are scheduled.

6. Discussion of growth processes with respect to existing data

In this section we briefly discuss our results with respect to the literature. We concentrate on new aspects and/or differences.

Concerning the stripes we could find no reports of annealing of Fe/Mo(110) films prior to our experiments. However several reports existed for annealed Fe/W(110) films, so that the question arises why self-organization of stripes had not been evidenced. In fact some wires were reported for Fe/W(110)[29, 86]. However these wires differ from ours by two aspects.

The first differing aspect is that the wires reported in the literature are always roughly oriented along [001], whatever the step orientation. The [001] orientation upon annealing is likely to result from anisotropic surface diffusion[6, 22] during the unwetting process. The reason why the atomic steps of the substrate were not effective is certainly that growth was performed at RT. In these conditions we have shown that grooves are not formed, so that the memory of the steps of the buffer surface is lost. In the case of Mo we evidenced a preferential alignement of nanostructures forming upon annealing films deposited at RT, for 2-3 AL (Figure 20a-b). This probably happens because this thickness is still comparable to the height of a step. However for W the steps can play no role because the preferred height is much larger than for Mo, so that at the minimum height required for the formation of stripes (2 nm, not illustrated with pictures here) the influence of buried steps is negligible. In recent experiments monitored *in situ* with LEEM we have shown that the formation of stripes is however easier along steps roughly parallel to [001], probably resulting from the anisotropic diffusion afore mentioned[57].

The second differing aspect if that the height of the reported stripes was generally larger than 5.5 nm. The height, width and spacing of the wires also varied with Θ and annealing conditions. This is typical for an annealing process without a preferred height. Incidentally, we sometimes observe such thicker wires amid the self-organized array. They seem to have grown at the expense of neighboring wires, and are therefore much thicker. The occurrence of such wires much depends on kinetics during the annealing.

Concerning islands there are several articles that report on them, both for W and Mo buffer layers. However as these were reported in the first stages of growth (with respect to our results), it is not straightforward to say to what type they belong, or even whether such a classification makes sense at all for small islands. The discussion should therefore be taken with care. First, all authors insist that their islands are wedge-shaped. Our compact islands are also wedge-shaped because their top is nearly atomically flat, however the wedge feature is in relative value not striking owing to the large thickness of the dots. Thus, the fact to be wedged does not provide a mean for discrimination. Let us now examine figures for the aspect ratio. The first report of wedge-shaped islands for Fe/W(110) is by Bethge *et al.* [11], upon growth at 300 °C. The average thickness of the islands remains around 1-1.5 nm so the comparison with both compact islands and the preferred height is difficult. $\eta \sim 0.01$ and $r \sim 1$ can be read from the published images. Wachowiak *et al.* also fabricated islands on W by depositing Fe at RT, followed

by annealing at $525 \pm 100\,^{\circ}$C[30]. The aspect ratios of the island studied are $\eta \sim 0.037$ and $r \sim 1.93$, *i.e.* compatible with the ranges of ratios found for our compact islands on W (Figure 15). Again on W, Röhlsberger *et al.* fabricated islands by depositing Fe at RT, followed by annealing at $425\,^{\circ}$C[31]. Quoting the authors the height of the islands is $h = 3.9 \pm 0.8$ nm. The vertical aspect ratio is $r \sim 0.019$, clearly out of the range from Figure 15, and the length is pretty much distributed, with η ranging from 1 to 5. The characteristics are thus closer to 'flat' islands, although the thickness is slightly smaller than what we report in this manuscript. Still on W, Sander *et al.* obtained thick wires aligned along [001]. Quoting these authors, these *were observed either after growth at 1000 K, or after annealing at 700-1000 K a room-temperature-grown Fe film.* Thus, there seems to be a contradiction with Röhlsberger for annealing around $425\,^{\circ}$C, unless the temperature calibration is different. Besides, we have never obtained wires by deposition at high temperature, so that this point is also unclear. Concerning Mo Malzbender *et al.* fabricated islands by deposition at $325\,^{\circ}$C. The islands have a *maximum height of 10 AL* which is very comparable to the report of Bethge *et al.* quoted above, and compatible with the preferred height we observe. Again on Mo, Murphy *et al.* came to similar results for deposition at $220\,^{\circ}$C. However their results may not be directly comparable since their substrate is more vicinal, with a terrace size around 20 nm.

To conclude the discussion, islands have been reported in the literature for both Fe/Mo and Fe/W, but at too early a stage to be unambiguously classified as 'compact' or 'flat'. Besides, some contradictory results are found between different reports in the literature, or between literature and our work. Therefore work is still needed to clarify the situation. When making comparison, one should also keep in mind that the characteristics of flat wedge-shaped islands (density, size, shape and orientation) are certainly influenced by the density and orientation of the atomic steps of the substrate, as it was clearly shown that these islands nucleate from the steps[16]. The examination of published data indeed shows that the density of dots increases with the density of atomic steps, and so at the same time the height of the dots for a given growth procedure decreases. An increased density of the nucleation of dots is a common feature, see *e.g.* [73]. Also, uncontrollable minute amounts of contaminants may play a role in the nucleation of stripes versus dots.

Finally, no data is available in the literature concerning the growth at very high temperature. The question why no compact islands grow from the beginning in this case is still open. One reason might be related to the high mobility of adatoms, causing the meeting of adatoms on the top of flat islands to be improbable. Thus, the nanostructures could grow only laterally by aggregation of adatoms and movement of kinks and steps. In the case of intermediate temperature, the non-hindered nucleation would be explained by the significant probability of adatoms to meet on top of the flat nanostructures and form a stable nucleus. It was also shown that adatom dynamics could vary by orders of magnitude in relation to strain[87]. It is therefore an open possibility that strain and stress at the edge of islands, which is known to be very high, plays a role.

7. Magnetic investigations

The growth and structural aspects of our investigations of Fe(110) self-assembled nanostructures, which were detailed above, had only been reported partly in previous papers. In contrast most of our studies of magnetic properties of Fe(110) have already been published[38, 88, 39, 89, 90]. Therefore we propose here only a condensed overview of our investigations. Details can be found in the original papers.

As a natural route to magnetic nanostructures we first investigated magnetic films[19]. The magnetic anisotropy of Fe/W(110) films with various capping layers had been extensively studied[91, 92, 93, 94, 95, 96, 97, 98, 99]. To the contrary, nearly no data was available for UHV-grown Fe/Mo(110) films nor W/Fe/W and Mo/Fe/Mo trilayers before our studies[19], apart from a report on Fe/Mo(110) multilayers, besides with significant uncertainties about surface anisotropy values[100]. Both W/Fe/W and Mo/Fe/Mo films keep their magnetization in-the-plane for any thickness. Thick Fe(110) films, typically several tens of nanometers, display a uniaxial anisotropy in-the-plane with [001] as an easy axis resulting from the projection of the bulk cubic anisotropy in the (110) plane. At lower thicknesses the relative contribution of interface-like anisotropy increases. For W/Fe/W films the interfacial contribution favors the $[1-10]$ axis, resulting in a reorientation transition around 10 nm, similarly to UHV/Fe/W(110) films[96, 97]. For Mo/Fe/Mo films the interfacial contribution favors the [100] axis. This strengthens the bulk anisotropy and thus does not give rise to a reorientation transition. Notice that this contrasts with uncapped structures, where Fe(1 AL) on calculations predict an easy axis along $[1-10]$ on both W(110)[101, 102] and Mo(110)[102], while only the former is document experimentally. Below $2-3$ nm the anisotropy becomes dominantly of second order with an anisotropy field around 0.5 T for 1 nm-thick films. We have checked that cc/Fe and Fe/cc interfaces induce a qualitatively similar change of interfacial anisotropy, *i.e.* of same sign and similar value[103]. Thus W/Fe/Mo and Mo/Fe/W films display a moderate total interfacial anisotropy, dominated by that of W. Thus, in principle using mixtures of Mo and W for buffer or capping layers should allow one to tune the effective anisotropy of Fe(110) layers independently from their thickness.

The first series of magnetic studies is concerned with thick stripes. Our interest in thick stripes arose from the fact that all self-organized systems reported so far had a height of one or two atomic layers[24, 23, 55, 76, 77, 78]. For such small dimensions thermal excitations become dominant over anisotropy, and no magnetic properties such as coercivity and remanence had been demonstrated at room temperature. A handwavy argument[33] shows that the effect of thermal excitations increases faster than interfacial anisotropy, so that the effect becomes ever more acute for smaller dimensions, as is reported[56, 78]. This argument remains valid whatever the type of interface be, surfaces, edges or kinks depending on the dimensionality. We issued a first report on irregular and discontinuous Mo/Fe/Mo stripes, with magnetic functionality at room temperature[38]. We improved the growth process of stripes, as reported above, which

resulted in the fabrication of continuous stripes of height in the range $3-5\,\mathrm{nm}$ with various buffer layers and cappings. For stripes aligned along [001], and buffer and capping interfaces made of Mo, both dipolar and interface anisotropy add up. This resulted in a coercivity up to $50\,\mathrm{mT}$ and a high remanence along the [001] direction. Stable magnetic domains of size a few hundreds of nanometers can be formed upon demagnetization along in-plane $[1-10]$[39].

The second series of magnetic studies is concerned with compact dots, mostly Mo/Fe/Mo. In the case of W/Fe/W in the range of thickness $[5-20\,\mathrm{nm}]$ the anisotropy is rather low and with a symmetry close to fourfold, owing to the occurrence of a reorientation transition, see the above paragraph dealing with the anisotropy of continuous films. Thus such dots are magnetically soft and display various types of flux-closure states[30, 104] expect in the ultrathin range[105]. The magnetic anisotropy is essentially uniaxial and stronger in the case of Mo/Fe/Mo in this range of thickness, so that the dots are mostly in a single domain state and display a significant remanence[35]. For a larger thickness Mo/Fe/Mo dots display flux-closure states. In the approximate range $[30-80\,\mathrm{nm}]$ both Landau (one single Bloch wall) and diamond (two or more vortices) states occur[88]. The shape of the domains is well reproduced by the two-dimensional model of Van den Berg[106, 107]. The observation of either a Landau or a diamond state in dots of similar shapes could be explained by the role of an asymmetry, like that of shape, during the demagnetization process: in a symmetric dot two vortices are created on opposite locii ending up in a diamond state, while only one vortex ending up in a Landau state may enter a significantly asymmetric dot[89]. For thicknesses in the range $[80-250\,\mathrm{nm}]$ only Landau states are found, which can be explained by the increasing cost of Néel walls, which are found in a diamond state. Besides, as the thickness of such dots is now comparable or larger than domain walls, the magnetization state varies along the thickness of the dot, and deviate from the model of Van den Berg. Magnetization flux closure can be evidenced both in-the-plane and along vertical cross-sections: these dots, although of size in the micrometer range, are premisses of bulk flux-closure states. This leads to unusual features like asymmetric Néel walls. These are forbidden in continuous films for such large thicknesses, but are stabilized in dots owing to the geometrical constraint. Such dots are therefore a model system to bridge the gap between simple nanostructure now well understood like thin flat dots, and bulk materials.

Conclusion

We have revisited the growth of Fe on W(110) and Mo(110) surfaces, to which this article is devoted. The first new key feature is that growth, which was already known to be of Stranski-Krastanov type, is here shown to be characterized by a bimodal distribution of islands. One species consists of compact facetted islands that grow homothetically during deposition, and whose shape can be understood with the Wulff-Kaischev construction. The interface energy between Fe and the substrate can be

extracted by analyzing the shape of the dots, which yields $\gamma_{\mathrm{int,Mo}} = 0.65 \pm 0.15\,\mathrm{J.m^{-2}}$ and $\gamma_{\mathrm{int,W}} = 0.10 \pm 0.05\,\mathrm{J.m^{-2}}$. Notice that these are effective values that include the strain energy located close to the interface, arising from the core and surroundings of interfacial misfit dislocations. The second species consists of thin flat islands with a preferred height: $1.4 \pm 0.2\,\mathrm{nm}$ for Fe/Mo and a broader distribution centered around 5.5 nm for Fe/W. Using W-Mo solid solutions we fabricated buffer layers whose lattice parameter can be continuously adjusted, and whose surface can be either pure W or pure Mo by using an ultrathin pseudomorphic capping layer. The preferred height is influenced by both parameters. Two possible origins for the preferred height are quantum-size effects and commensurate/discommensurate transition of the interfacial dislocations network. Further works is needed to determine which effect is relevant. Finally, we took advantage of the preferred height to fabricate arrays of nanometers-thick stripes self-organized along the atomic steps of the buffer layer. The orientation and separation of the stripes can be adjusted by controlling the miscut angle and azimuth, their width by the amount of material deposited, and their height can be controlled via slight variations of the lattice parameter of solid-solution buffer layers.

As an outlook we believe that the principle of growing buffer layers of solid solutions A_xB_{1-x} with a full range of x from 0 to 1, which we named *chemical wedge* or *chemical gradient layer* (CGL), is a promising tool. This process is inspired from the concept of wedges of *thickness* that is nowadays used by many groups, which allows one to perform quick and systematic studies of the influence of thickness of some feature, be it of growth or of a physical property. Chemical wedged should allow the study of the effects related to misfit, either for growth or physical properties.

Appendix I

The Wulff-Kaischev construction relates the occurrence and geometry of the facets arising in a supported crystal, with the values of surface and interface energies [Eq. (1)]. Based on this construction, straightforward calculations yield the vertical and lateral aspect ratios expected for bcc(110) supported crystal. If only {110} and {001} facets are considered one finds:

- For $0 < \gamma_{\mathrm{int}} < \gamma_{\{110\}}(\sqrt{2}-1)$ $(\simeq 1\,\mathrm{J/m^2})$

$$r = \frac{L}{l} = \frac{1}{\sqrt{2}} \frac{(\gamma_{\mathrm{int}} + \gamma_{\{110\}})}{(\gamma_{\mathrm{int}} - \gamma_{\{110\}} + \sqrt{2}\gamma_{\{001\}})} \tag{2}$$

$$\eta = \frac{h}{l} = \frac{1}{2} \frac{\gamma_{\mathrm{int}}}{(\gamma_{\mathrm{int}} - \gamma_{\{110\}} + \sqrt{2}\gamma_{\{001\}})} \tag{3}$$

- For $\gamma_{\{110\}}(\sqrt{2}-1) < \gamma_{\mathrm{int}} < 2\gamma_{\{110\}} - \sqrt{2}\gamma_{\{001\}}$ $(\simeq 1.72\,\mathrm{J/m^2})$

$$r = \frac{L}{l} = \frac{\gamma_{\{110\}}}{(\gamma_{\mathrm{int}} - \gamma_{\{110\}} + \sqrt{2}\gamma_{\{001\}})} \tag{4}$$

$$\eta = \frac{h}{l} = \frac{1}{2} \frac{\gamma_{\mathrm{int}}}{(\gamma_{\mathrm{int}} - \gamma_{\{110\}} + \sqrt{2}\gamma_{\{001\}})} \tag{5}$$

- For $2\gamma_{\{110\}} - \sqrt{2}\gamma_{\{001\}} < \gamma_{\rm int} < \gamma_{\{110\}}$ $(= 2.43\,{\rm J/m^2})$

$$r = \frac{L}{l} = 1 \tag{6}$$

$$\eta = \frac{h}{l} = \frac{\gamma_{\rm int}}{2\gamma_{\{110\}}}. \tag{7}$$

More general formulae taking into account {310} and {211} facets are given in Ref.[108]. In the case of Fe(110) these change only slightly the value of r, while η remains nearly unchanged. The numerical values (Figure 15) are derived using the surface energies computed in Ref[3].

Appendix II

In this appendix we calculate the angles β (with respect to the substrate plane) of the possible facets of bcc(110) dots for various azimuths of the electron beam. Let us write $\mathbf{a} = a\mathbf{i}$, $\mathbf{b} = a\mathbf{j}$ and $\mathbf{c} = a\mathbf{k}$ the three vectors of the cubic cell in real space, $\mathbf{a}^* = (2\pi/a)\mathbf{i}$, $\mathbf{b}^* = (2\pi/a)\mathbf{j}$ and $\mathbf{c}^* = (2\pi/a)\mathbf{k}$ the reciprocal lattice vectors. Let us write a scattering vector in the general form: $\mathbf{q} = h\mathbf{a}^* + k\mathbf{b}^* + l\mathbf{c}^*$. Only the nodes for which $h+k+l \equiv 0[2]$ arise for a simple centered cubic cell. For a given azimuth $\mathbf{R}$ RHEED patterns may arise only from facets on which the electron beam impinges at grazing incidence, that is for $\mathbf{q}.\mathbf{R} = 0$. The cases of three azimuths are treated below, for which facets indeed arise for our Fe(110) dots.

7.1. Azimuth [001]

Let us look for planes determined by $\mathbf{q}.\mathbf{c} = 0$, thus satisfying $l = 0$. The general index of these is thus $(hk0)$ with $h + k \equiv 0[2]$. One has $\cos\beta = (h+k)/\sqrt{2(h^2+k^2)}$, $\sin\beta = (h-k)/\sqrt{2(h^2+k^2)}$ and $\tan\beta = (h-k/h+k)$. The features of the main facets are reported in Table 2.

Table 2. Angles of the main possible facets for the electron beam azimuth [001].

(hk)	Plane (hkl)	Angle with surface
(24)	(240)	$\sim 18.43\,^\circ$
(13)	(130)	$\sim 26.57\,^\circ$
(02)	(020)	$45\,^\circ$

7.2. Azimuth $[1-10]$

Let us look for planes determined by $\mathbf{q}.(\mathbf{a}-\mathbf{b}) = 0$, thus satisfying $h = k$. The general index of these is thus (hhl) with $2h + l \equiv 0[2]$. One has $\cos\beta = 2h/\sqrt{2(2h^2+l^2)}$, $\sin\beta = l/\sqrt{2h^2+l^2}$ and $\tan\beta = l/(h\sqrt{2})$. The features of the main facets are reported in Table 3.

Table 3. Angles of the main possible facets for the electron beam azimuth $[1-10]$.

(hl)	Plane (hkl)	Angle with surface
$(3\overline{2})$	$(33\overline{2})$	$\sim 25.23\,^\circ$
$(2\overline{2})$	$(22\overline{2})$	$\sim 35.26\,^\circ$
$(1\overline{2})$	$(11\overline{2})$	$\sim 54.74\,^\circ$

7.3. Azimuth $[1-1-1]$

Let us look for planes determined by $\mathbf{q}.(\mathbf{a}-\mathbf{b}-\mathbf{c})=0$, thus satisfying $h-k=l$. The general index of these is thus $(h,k,h-k)$ with $2h \equiv 0[2]$, so with no restriction on h. One has $\cos\beta = (h+k)/[2\sqrt{(h^2+k^2-hk)}]$, $\sin\beta = (\sqrt{3}/2)(h-k)/\sqrt{h^2+k^2-hk}$ and $\tan\beta = (\sqrt{3})(h-k/h+k)$. The features of the main facets are reported in Table 4.

Table 4. Angles of the main possible facets for the electron beam azimuth $[1-1-1]$.

(hk)	Plane (hkl)	Angle with surface
(23)	$(23\overline{1})$	$\sim 19.11\,^\circ$
(12)	$(12\overline{1})$	$30\,^\circ$
(13)	$(13\overline{2})$	$\sim 40.89\,^\circ$
(01)	$(01\overline{1})$	$60\,^\circ$

Acknowledgments

We are happy to acknowledge technical help concerning electronics (S. Biston, S. Pelle), XRD (L. Ortega) wafer and target preparation (D. Barral, K. Ayadi, R. Haettel). Concerning magnetism, we acknowledge the contribution of co-authors in the articles cited in the present condensed presentation: J. C. Toussaint, B. Kevorkian, Y. Samson, J. Vogel, A. Locatelli, A. Ballestrazzi, W. Wernsdorfer, R. Hertel, J. Kirschner, D. Mailly, S. Cherifi, S. Heun. We are finally grateful to B. Canals and M. Taillefumier for help with Mathematica.

This work was partly funded by *Région Rhône-Alpes* (Emergence 2001) and the French ministry of Research (ACI Nanostructures 2000).

References

[1] U. Gradmann and G. Waller, Surf. Sci. **116**, 539 (1982).
[2] M. Tikhov and E. Bauer, Surf. Sci. **232**, 73 (1990).
[3] L. Vitos, A. V. Ruban, H. L. Skiver, and J. Kollár, Surf. Sci. **411**, 186 (1998).
[4] J. Malzbender, M. Przybylski, J. Giergiel, and J. Kirschner, Surf. Sci. **414**, 187 (1998).
[5] J. Kolaczkiewicz and E. Bauer, Surf. Sci. **450**, 106 (2000).
[6] D. Reuter, G. Gerth, and J. Kirschner, Phys. Rev. B **57**, 2520 (1998).
[7] M. Sladecek, B. Sepiol, J. Korecki, T. Slezak, R. Rüffer, D. Kmiec, and G. Vogl, Surf. Sci. **566-568**, 372 (2004).

[8] P. O. Jubert, O. Fruchart, and C. Meyer, Surf. Sci. **522**, 8 (2003).
[9] T. M. Gardiner, Thin Solid Films **105**, 213 (1983).
[10] H. J. Elmers, J. Hauschild, H. Höche, U. Gradmann, H. Bethge, D. Heuer, and U. Köhler, Phys. Rev. Lett. **73**, 989 (1994).
[11] H. Bethge, D. Heuer, C. Jensen, K. Reshöft, and U. Köhler, Surf. Sci. **331-333**, 878 (1995).
[12] D. Sander, A. Enders, and J. Kirschner, Europhys. Lett. **45**, 208 (1999).
[13] H. L. Meyerheim, D. Sander, R. Popescu, and J. Kirschner, Phys. Rev. B **64**, 045414 (2001).
[14] M. Bode, R. Pascal, M. Dreyer, and R. Wiesendanger, Phys. Rev. B **54**, R8385 (1996).
[15] R. Popescu, H. L. Meyerheim, D. Sander, J. Kirschner, P. Steadman, O. Robach, and S. Ferrer, Phys. Rev. B **68**, 155421 (2003).
[16] S. Murphy, D. Mac Mathúna, G. Mariotto, and I. V. Shvets, Phys. Rev. B **66**, 195417 (2002).
[17] Y. Maehara, A. Yamada, H. Kawanowa, and Y. Gotoh, Appl. Surf. Sci. **237**, 316 (2004).
[18] B. M. Clemens, R. Osgood, A. P. Payne, B. M. Lairson, S. Brennan, R. L. White, and W. D. Nix, J. Magn. Magn. Mater. **121**, 37 (1993).
[19] O. Fruchart, J.-P. Nozières, and D. Givord, J. Magn. Magn. Mater. **207**, 158 (1999).
[20] M. Albrecht, H. Fritzsche, and U. Gradmann, Surf. Sci. **294**, 1 (1993).
[21] O. Fruchart, S. Jaren, and J. Rothman, Appl. Surf. Sci. **135**, 218 (1998).
[22] U. Köhler, C. Jensen, C. Wolf, A. C. Schindler, L. Brendel, and D. Wolf, Surf. Sci. **454-456**, 676 (2000).
[23] J. Hauschild, U. Gradmann, and H. J. Elmers, Appl. Phys. Lett. **72**, 3211 (1998).
[24] J. Hauschild, H. J. Elmers, and U. Gradmann, Phys. Rev. B **57**, R677 (1998).
[25] H. Elmers, J. Hauschild, and U. Gradmann, J. Magn. Magn. Mater. **221**, 219 (2000).
[26] P. J. Berlowitz, J. W. He, and D. W. Goodman, Surf. Sci. **231**, 315 (1990).
[27] D. Sander, R. Slomski, A. Enders, C. Schmidthals, D. Reuter, and J. Kirschner, J. Phys. D: Appl. Phys. **31**, 663 (1998).
[28] D. Sander, A. Enders, C. Schmidthals, D. Reuter, and J. Kirschner, Surf. Sci. **402-404**, 351 (1998).
[29] D. Sander, Rep. Prog. Phys. **62**, 809 (1999).
[30] A. Wachowiak, J. Wiebe, M. Bode, O. Pietzsch, M. Morgenstern, and R. Wiesendanger, Science **298**, 577 (2002).
[31] R. Röhlsberger, J. Bansmann, V. Senz, K. L. Jonas, A. Bettac, and K. H. Meiwes-Broer, Phys. Rev. B **67**, 245412 (2003).
[32] V. Usov, S. Murphy, and I. Shvets, J. Magn. Magn. Mater. **286**, 18 (2005).
[33] O. Fruchart, C. R. Physique **6**, 61 (2005).
[34] J. Shen, Zheng Gaib, and J. Kirschner, Surf. Sci. Rep. **52**, 163 (2004).
[35] P.-O. Jubert, O. Fruchart, and C. Meyer, Phys. Rev. B **64**, 115419 (2001).
[36] P. O. Jubert, O. Fruchart, and C. Meyer, J. Magn. Magn. Mater. **226-230**, 1842 (2001).
[37] O. Fruchart, P.-O. Jubert, C. Meyer, M. Klaua, J. Barthel, and J. Kirschner, J. Magn. Magn. Mater. **239**, 224 (2002).
[38] P.-O. Jubert, O. Fruchart, and C. Meyer, J. Magn. Magn. Mater. **242-245**, 565 (2002).
[39] O. Fruchart, M. Eleoui, J. Vogel, P.-O. Jubert, A. Locatelli, and A. Ballestrazzi, Appl. Phys. Lett. **84**, 1335 (2004).
[40] N. Cherief, D. Givord, O. McGrath, Y. Otani, and F. Robaut, J. Magn. Magn. Mater. **126**, 225 (1993).
[41] G. C. Tyrrell, T. York, N. Cherief, D. Givord, J. Lawler, J. G. Lunney, M. Buckley, and I. W. Boyd, Microelec. Engineer. **25**, 247 (1994).
[42] S. Pokrant, O. Fruchart, C. Meyer, and L. Ortega, Surf. Sci. **506**, 235 (2002).
[43] Y. Nishihata, M. Nakayama, H. Kato, N. Sano, and H. Terauchi, J. Appl. Phys. **60**, 3523 (1986).
[44] S. Rusponi, G. Costantini, F. Buatier de Mongeot, C. Boragno, and U. Valbusa, Appl. Phys. Lett. **75**, 3318 (1999).
[45] U. Valbusa, C. Boragno, and F. Buatier de Mongeot, J. Phys.: Cond. Mat. **14**, 8153 (2002).

[46] D. Sekiba, R. Moroni, G. Gonella, F. Buatier de Mongeot, C. Boragno, L. Mattera, and U. Valbusa, Appl. Phys. Lett. **84**, 762 (2003).
[47] W. Święçh, M. Mundschau, and C. Flynn, Surf. Sci. **437**, 61 (1999).
[48] U. May, R. Calarco, J. O. Hauch, H. Kittur, M. Fonine, U. Rüdiger, and G. Güntherodt, Surf. Sci. **489**, 144 (2001).
[49] M. Fonin, Y. S. Dedkov, J. Mayer, U. Rüdiger, and G. Güntherodt, Phys. Rev. B **68**, 045414 (2003).
[50] D. A. Valdaitsev, A. Kukunin, J. Prokop, H. J. Elmers, and G. Schönhense, Appl. Phys. A **80**, 731 (2005).
[51] M. Fraune, J. O. Hauch, G. Güntherodt, M. Laufenberg, M. Fonin, U. Rüdiger, J. Mayer, and P. Turban, J. Appl. Phys. **99**, 033904 (2006).
[52] P. Turban, S. Andrieu, B. Kierren, E. Snoeck, C. Teodorescu, and A. Traverse, Phys. Rev. B **65**, 134417 (2002).
[53] P. Y. Friot, P. Turban, S. Andrieu, M. Piecuch, E. Snoeck, A. Traverse, E. Foy, and C. Theodorescu, Europhys. J. D **15**, 41 (2000).
[54] P. Müller and R. Kern, Surf. Sci. **457**, 229 (2000).
[55] J. Shen, R. Skomsky, M. Klaua, H. Jenniches, S. S. Manoharan, and J. Jirschner, Phys. Rev. B **56**, 2340 (1997).
[56] P. Gambardella, A. Dallmeyer, K. Maiti, M. C. Malagoli, W. Eberhardt, K. Kern, and C. Carbone, Nature **416**, 301 (2002).
[57] F. Cheynis, N. Rougemaille, O. Fruchart, and A. K. Schmid, Surf. Sci. (2006), submitted.
[58] J. Camarero, T. Graf, J. J. de Miguel, R. Miranda, W. Kuch, M. Zharnikov, A. Dittschar, C. M. Schneider, and J. Kirschner, Phys. Rev. Lett. **76**, 4428 (1996).
[59] F. Bisio, R. Moroni, M. Canepa, L. Mattera, R. Bertacco, and F. Ciccacci, Phys. Rev. Lett. **83**, 4868 (1999).
[60] J. Ferrón, L. Gómez, J. M. Gallego, J. Camarero, J. E. Prieto, V. Cros, A. L. Vázquez de Parga, J. J. de Miguel, and R. Miranda, Surf. Sci. **459**, 135 (2000).
[61] P. O. Jubert, S. Jaren, and C. Meyer, in *Magnetic storage systems beyond 2000*, Vol. 41 of *NATOSCIENCE SERIES II: Mathematics, Physics and Chemistry*, edited by G. C. Hadjipanayis (Kluwer Academic Publishers, Dordrecht, The Netherlands., 2001), experiment growth magnetism Self-assembled magnetic nanostructures: Fe islands on a Mo(110) surface.
[62] A. Stenborg and E. Bauer, Surf. Sci. **135**, 394 (1987).
[63] A. Stenborg and E. Bauer, Surf. Sci. **189-190**, 570 (1987).
[64] A. Stenborg, J. N. Andersen, O. Björneholm, A. Nilsson, and N. Mårtensson, Phys. Rev. Lett. **63**, 187 (1989).
[65] A. Stenborg, O. Björneholm, A. Nilsson, N. Mårtensson, J. N. Andersen, and C. Wigren, Phys. Rev. B **40**, 5916 (1989).
[66] A. R. Smith, K.-J. Chao, Q. Niu, and C.-K. Shih, Science **273**, 226 (1996).
[67] I. B. Altfeder, K. A. Matveev, and D. M. Chen, Phys. Rev. Lett. **78**, 2815 (1997).
[68] V. Yeh, L. Berbil-Bautista, C. Z. Wang, K. M. Ho, and M. C. Tringides, Phys. Rev. Lett. **85**, 5158 (2000).
[69] W. B. Su, S. H. Chang, W. B. Jian, C. S. Chang, L. J. Chen, and T. T. Tsong, Phys. Rev. Lett. **86**, 5116 (2001).
[70] L. Gavioli, K. R. Kimberlin, M. C. Tringides, J. F. Wendelken, and Z. Zhang, Phys. Rev. Lett. **82**, 129 (1999).
[71] L. Huang, S. Jay Chey, and J. Weaver, Surf. Sci. **616**, L1101 (1998).
[72] D. A. L. T. Miller, J. J. Paggel, M. Y. Chou, and T. C. Chiang, Science **292**, 1131 (2001).
[73] R. Otero, A. L. Vázquez de Parga, and R. Miranda, Phys. Rev. B **66**, 115401 (2002).
[74] V. Repain, G. Baudot, H. Ellmer, and S. Rousset, Mater. Sci. Engrg. B **96**, 178 (2002).
[75] W. L. Ling, T. Giessel, K. Thürmer, R. Q. Hwang, N. C. Bartelt, and K. F. McCarty, Surf. Sci. **570**, L297L303 (2004).

[76] B. Voigtländer, G. Meyer, and N. M. Amer, Phys. Rev. B **44**, 10354 (1991).
[77] B. Voigtländer, G. Meyer, and N. M. Amer, Surf. Sci. Lett. **255**, L529 (1991).
[78] P. Gambardella, J. Phys.: Cond. Mat. **15**, S2533 (2003).
[79] S. Cherifi, C. Boeglin, S. Stanescu, J. P. Deville, C. Mocuta, H. Magnan, P. Le Fèvre, P. Ohresser, and N. B. Brookes, Phys. Rev. B **64**, 184405 (2001).
[80] J. de la Figuera, Prieto, C. Ocal, and R. Miranda, Phys. Rev. B **47**, 13043 (1993).
[81] J. de la Figuera, J. E. Prieto, G. Kostka, S. Müller, C. Ocal, R. Miranda, and K. Heinz, Surf. Sci. **349**, L139 (1996).
[82] M. O. Pedersen, I. A. Bönicke, E. L. sgaard, I. Stensgaard, A. Ruban, J. A. N. rsov, and F. Besenbacher, Surf. Sci. **387**, 86 (1997).
[83] P. Müller and A. Saúl, Surf. Sci. Rep. **54**, 157 (2005).
[84] Y. W. Mo, D. E. Savage, B. S. Schwartentruber, and M. G. Lagally, Phys. Rev. Lett. **65**, 1020 (1990).
[85] J. A. Floro, E. Chason, L. B. Freund, R. D. Twesten, R. Q. Hwang, and G. A. Lucadamo, Phys. Rev. B **59**, 1990 (1999).
[86] N. Rougemaille and A. K. Schmid, J. Appl. Phys. **99**, 08S502 (2006).
[87] D. V. Tsivlin, V. S. Stepanyuk, W. Hergert, , and J. Kirschner, Phys. Rev. B **68**, 205411 (2003).
[88] P. O. Jubert, J. C. Toussaint, O. Fruchart, C. Meyer, and Y. Samson, Europhys. Lett. **63**, 135 (2003).
[89] O. Fruchart, J. C. Toussaint, P.-O. Jubert, W. Wernsdorfer, R. Hertel, J. Kirschner, and D. Mailly, Phys. Rev. B **70**, 172409 (2004), brief Report.
[90] R. Hertel, O. Fruchart, S. Cherifi, P.-O. Jubert, S. Heun, A. Locatelli, and J. Kirschner, Phys. Rev. B **72**, 214409 (2005).
[91] U. Gradmann, J. Korecki, and G. Waller, Appl. Phys. A **A39**, 101 (1986).
[92] B. Hillebrands, P. Baumgart, and G. Güntherodt, Phys. Rev. B **36**, 2450 (1987).
[93] H. J. Elmers and U. Gradmann, Appl. Phys. A **A51**, 255 (1990).
[94] P. Baumgart, B. Hillebrands, and G. Guntherodt, J. Magn. Magn. Mater. **93**, 225 (1991).
[95] H. J. Elmers, T. Furubayashi, M. Albrecht, and U. Gradmann, J. Appl. Phys. **70**, 5764 (1991).
[96] U. Gradmann, in *Handbook of magnetic materials*, edited by K. H. J. Buschow (Elsevier Science Publishers B. V., North Holland, 1993), Vol. 7, Chap. 1, pp. 1–96.
[97] F. Gerhardter, Y. Li, and K. Baberschke, Phys. Rev. B **47**, 11204 (1993).
[98] H. Fritzsche, H. J. Elmers, and U. Gradmann, J. Magn. Magn. Mater. **135**, 343 (1994).
[99] H. J. Elmers and U. Gradmann, Surf. Sci. **304**, 201 (1994).
[100] R. M. Osgood III, R. L. White, and B. M. Clemens, Mat. Res. Soc. Symp. Proc. **384**, 209 (1995).
[101] I. Galanakis, M. Alouani, and H. Dreysse, Phys. Rev. B **62**, 3923 (2000).
[102] W. Qian and W. Hübner, Phys. Rev. B **64**, 092402 (2001).
[103] O. F. *et al.*, unpublished.
[104] M. Bode, A. Wachowiak, J. Wiebe, A. Kubetzka, M. Morgenstern, and R. Wiesendanger, Appl. Phys. Lett. **84**, 948 (2004).
[105] U. Ramsperger, A. Vaterlaus, U. Maier, and D. Pescia, Appl. Surf. Sci. **130-132**, 889 (1998).
[106] H. A. M. Van den Berg, J. Magn. Magn. Mater. **44**, 207 (1984).
[107] H. A. M. Van den Berg, J. Appl. Phys. **60**, 1104 (1986).
[108] P. O. Jubert, Ph.D. thesis, Université Joseph Fourier, Grenoble, 2001.